Check for updates

Advanced Energy Materials

ADVANCED ENERGY MATERIALS
www.advenergymat.de

RESEARCH ARTICLE OPEN ACCESS

Stabilizing Magnesium Anodes in Rechargeable Magnesium Batteries via Fluorinated Cyclic Ether Electrolyte Additive

Hafiz Ahmad Ishfaq[1,2,3] | Andrijana Marojević[1,2] | Carolina Cruz Cardona[4,5] | Gregor Kapun[1,2] | Elena Tchernychova[1] | Olivera Lužanin[1] | Jan Bitenc[1] | Miran Gaberšček[1,2] | Robert Dominko[1,2,3] | Sara Drvarič Talian[1,2]

[1]Department of Materials Chemistry, National Institute of Chemistry, Ljubljana, Slovenia | [2]Faculty of Chemistry and Chemical Technology, University of Ljubljana, Ljubljana, Slovenia | [3]ALISTORE – European Research Institute, Amiens, Cedex, France | [4]Department of Engineering, King's College London, London, UK | [5]The Faraday Institution, Quad One, Harwell Science and Innovation Campus, Didcot, UK

Correspondence: Sara Drvarič Talian (sara.drvarictalian@ki.si)

Received: 12 November 2025 | **Revised:** 10 February 2026 | **Accepted:** 24 February 2026

Keywords: electrochemical impedance spectroscopy | fluorinated electrolyte | Magnesium metal anode | weakly coordinating salt

ABSTRACT

Rechargeable magnesium batteries (RMBs) are gaining significant attention as next-generation energy storage due to high theoretical volumetric energy density, abundance, and low cost of Mg metal. However, practical development remains constrained by surface passivation, cycling instability, and scarcity of compatible electrolytes. In this study, we explore the incorporation of fluorinated cyclic ethers in $Mg[Al(hfip)_4]_2$/diglyme-based electrolytes. The addition of 10 vol.% fluorinated cyclic ether improves the electrochemical performance of Mg metal, evidenced by improved coulombic efficiency (98.2% to 99.1%), cycling life (15 vs 90 cycles of Mg plating/stripping at 2 mA cm^{-2} and 2 mAh cm^{-2}), and oxidative stability (3.7 V to 4.1 V vs Mg^0/Mg^{2+}). The optimized electrolyte also enables stable and prolonged cycling in high-voltage Mg||polyaniline cells, achieving 75% capacity retention over 500 cycles at 1C. *Operando* electrochemical impedance spectroscopy, supplemented by scanning electron microscopy and X-ray photoelectron spectroscopy, was employed to explain the improvement. The electrochemical bottleneck processes occurring on the Mg metal anode without fluorinated ether addition were determined to be incomplete electrode activation, high surface area deposits formed during plating, and passivation of such deposits. These findings highlight the potential of fluorinated ether additives in improving Mg metal performance and advancing electrolyte design for next-generation RMBs.

1 | Introduction

Driven by the growing demand for energy storage systems with higher energy density, lower cost, and improved sustainability, research interest in non-lithium based energy storage technologies has intensified in recent years [1, 2]. Among these, rechargeable magnesium batteries (RMBs) have gained significant attention due to the natural abundance of Mg, which is over 1000 times greater than that of Li [3, 4]. Furthermore, Mg metallic anodes offer a high theoretical volumetric energy density of 3833 mAh cm^{-3}, compared to 2061 mAh cm^{-3} for Li metal [5], and exhibit a relatively low reduction potential (−2.38 V vs SHE). Although the formation of Mg dendrites has been reported in some studies [6–8], Mg is generally considered less prone to dendritic growth than Li [9]. This characteristic suggests that RMBs could potentially serve as safer electrochemical energy storage devices compared to Li metal batteries [10]. However, due to the thermodynamic instability of Mg metal, most electrolytes and impurities readily undergo decomposition on its surface, forming resistive passive layers that hinder reversible Mg plating and stripping [11–14]. For instance, surface films formed by conventional electrolytes containing strongly coordinating ionic

This is an open access article under the terms of the Creative Commons Attribution License, which permits use, distribution and reproduction in any medium, provided the original work is properly cited.

© 2026 The Author(s). *Advanced Energy Materials* published by Wiley-VCH GmbH

salts, such as $Mg(ClO_4)_2$ [15] and $Mg(BF_4)_2$ [16] in solvents like carbonates and nitriles, exhibit high resistivity. This results in significant voltage hysteresis (~2.0 V), even under low current densities, thereby limiting the electrochemical performance of RMBs [17, 18]. Some Mg electrolytes therefore, depend on chloride species in high concentration to corrode the Mg surface and facilitate reversible Mg plating and stripping. These chloride-based electrolytes, however, exhibit limited oxidative stability (~2.5 V vs Mg^{2+}/Mg^0) and are highly corrosive to current collectors and battery casings, posing significant challenges for practical applications [19].

Therefore, research and development efforts in RMB electrolytes are primarily focused on improving the cycling efficiency of the Mg metal anode while simultaneously expanding the electrolyte's electrochemical stability window to enable the operation of high-voltage cathodes. Although substantial recent work has been devoted to modifying the Mg metal anode surface through artificial coatings to facilitate RMB operation under aggravated conditions [20–22], electrolyte engineering remains critically underdeveloped. In this context, the development of intrinsically stable electrolytes is essential for realizing high-voltage RMBs without relying on complex anode surface modifications. To address these challenges, chloride-free Mg salts incorporating bulky fluorinated carborane [23] or alkoxyborate [24, 25] /aluminate [26, 27] anions have been developed. These electrolytes exhibit high reversibility for Mg plating and stripping, achieving coulombic efficiencies exceeding 99%. Among these, our group recently utilized magnesium 1,1,1,3,3,3-hexafluoroisopropoxy (hfip) aluminate salt, $Mg[Al(hfip)_4]_2$, dissolved in diethylene glycol dimethyl ether (diglyme or G2) electrolyte [27, 28]. This electrolyte demonstrated improved performance, achieving a high coulombic efficiency (>99%) and significantly reduced overpotentials (~50 mV) for Mg plating/stripping, making it a promising electrolyte for RMBs. However, to the best of our knowledge, its long-term stability at higher current densities and operation at high voltages have not yet been reported. One of the primary challenges limiting the high-voltage operation of these electrolytes is their low oxidative stability. It has been demonstrated that the fundamental constraint on oxidative stability primarily originates from the ethereal solvents commonly used in Mg electrolytes [29].

In this regard, solvent engineering has emerged as a promising strategy to further enhance the long-term cycling stability and oxidative stability of $Mg[Al(hfip)_4]_2$-based electrolytes, particularly to mitigate solvent decomposition under prolonged cycling at high current densities and voltages [30, 31]. An ideal solvent for high-performance RMBs must satisfy the essential criteria of: (i) a high solvating ability to dissolve Mg salts effectively and (ii) a high electrochemical stability window for RMBs to work at higher current rates and against high voltage cathodes. However, simultaneously achieving these properties within a single solvent remains a significant challenge. G2 has been widely utilized to facilitate the dissociation of Mg salts due to its multi-dentate coordination with Mg^{2+} cations. While it effectively promotes ion dissociation, it also induces large overpotentials and limits cycle life, especially at high current densities and voltages [29, 32].

Recently, hydrofluoroethers (HFEs) have been incorporated into electrolytes for alkali metal batteries as diluents, significantly improving cycling performance under high current densities and voltages [33–35]. In the context of RMB electrolytes, the primary challenge in replacing ethereal solvents with fluorinated solvents lies in their inability to support reversible Mg cycling. This limitation stems from their reductive instability and the absence of an effective interphase on the Mg anode, which is essential for facilitating stable Mg plating and stripping [29]. To date, only four studies have reported the use of HFEs as *co-solvents* in $MgCl_2$- and magnesium bis(trifluoromethanesulfonimide) ($Mg(TFSI)_2$)-based electrolytes that enable effective Mg plating/stripping [29, 31, 36, 37]. Among these, only one study, conducted by the Mandai group [36], has explored the use of various linear fluorinated ethers as main solvents in combination with fluorinated alkoxyborate/aluminate salts to improve the anodic stability of RMB electrolyte, but its compatibility with high-voltage cathode was not reported. Another critical challenge in RMBs is the limited understanding of the electrochemical processes occurring at the Mg metal anode in contact with these electrolytes [14]. Gaining deeper insights into these processes is essential for the rational design and development of efficient Mg electrolytes.

In this study, we address these challenges by strategically incorporating a small fraction of cyclic HFE, 2,2-bis(trifluoromethyl)-1,3-dioxolane (hereafter referred to as FDOL), into the $Mg[Al(hfip)_4]_2$/G2 electrolyte. The objective is to enhance its oxidative stability and long-term cycling performance under high current densities and voltages, as well as to gain a deeper understanding of the electrochemical processes occurring at the Mg metal anode. $Mg[Al(hfip)_4]_2$ salt was selected due to its non-corrosive nature, high ionic conductivity, and improved Mg plating/stripping efficiency with reduced overpotentials compared to $Mg(TFSI)_2$ and chloride-based salts. We selected FDOL as a representative cyclic fluorinated ether based on several Mg-relevant considerations: (i) its cyclic structure and reduced conformational freedom, which favor weak Mg^{2+} coordination; (ii) its relatively low donor number compared to diglyme, which minimizes competitive solvation; and (iii) its high oxidative stability to support Mg metal performance at high voltages and current densities, previously demonstrated in Li metal batteries [38]. We demonstrate that the incorporation of only 10 vol.% FDOL into the $Mg[Al(hfip)_4]_2$/G2 electrolyte significantly improves the electrochemical performance of the Mg metal anode and high-voltage Mg||polyaniline cells. To gain mechanistic insights, we employed *operando* electrochemical impedance spectroscopy (EIS) to investigate the electrochemical processes occurring at the Mg metal anode and suggested the possible mechanisms leading to the improvement of Mg metal anode performance when using FDOL-based electrolytes.

2 | Results and Discussion

To explore the performance of fluorinated ether-based electrolytes in Mg metal batteries, initial experiments were conducted by attempting to use pure FDOL as the electrolyte solvent. Although $Mg[Al(hfip)_4]_2$ could be dissolved in pure FDOL, this electrolyte was not able to plate and strip Mg in Mg||Pt cells (Note S1 and Figures S1 and S2), so we aimed to create hybrid electrolytes by mixing G2 and FDOL with 0.4 M $Mg[Al(hfip)_4]_2$ salt. We selected a salt concentration of 0.4 M based on our recent work, in which Marojević et al. systematically investigated the effect of $Mg[Al(hfip)_4]_2$ concentration in G2 solvent, where we

16146840, 2026, 18, Downloaded from https://advanced.onlinelibrary.wiley.com/doi/10.1002/aenm.202506415 by Ervin Rems - Bibliothèque de Sorbonne Université , Wiley Online Library on [15/05/2026]. See the Terms and Conditions (https://onlinelibrary.wiley.com/terms-and-conditions) on Wiley Online Library for rules of use; OA articles are governed by the applicable Creative Commons License

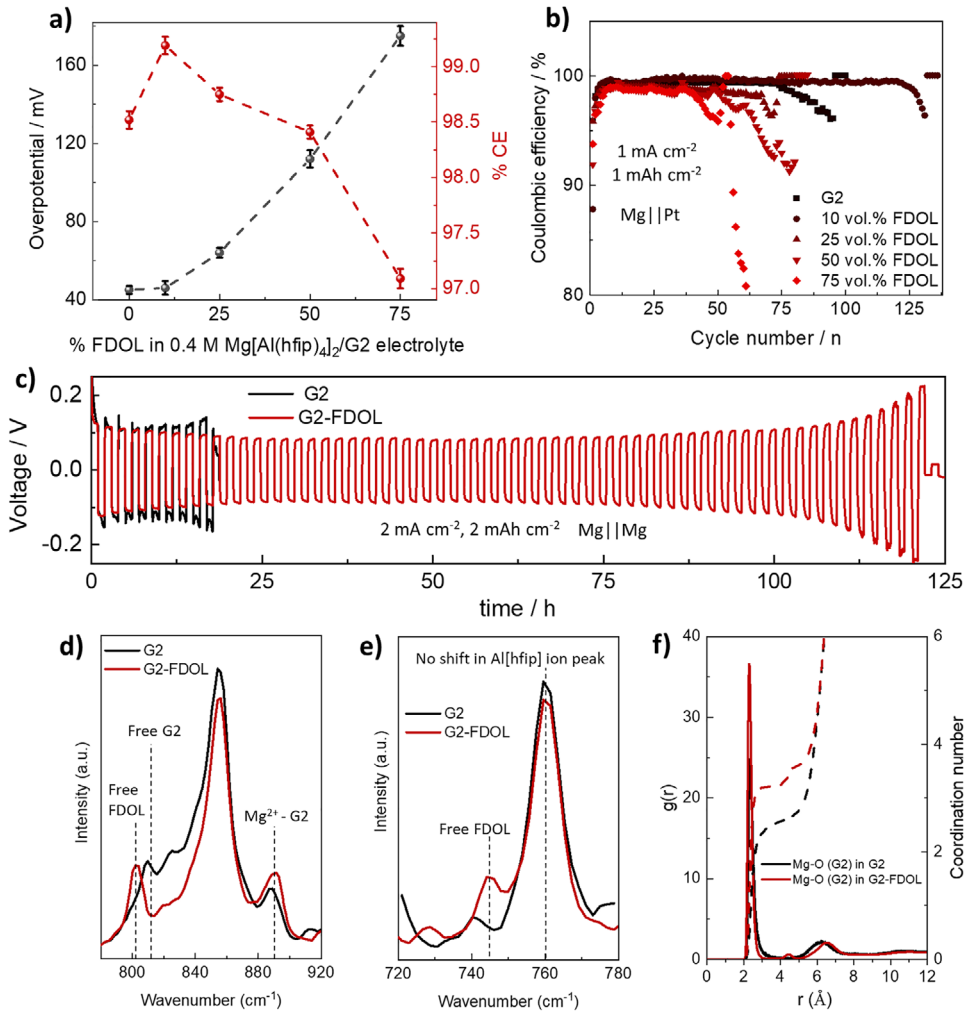

FIGURE 1 | (a) Influence of varying FDOL content on overpotentials, CE, and (b) cycling stability of 0.4 M $Mg[Al(hfip)_4]_2$ in G2 electrolyte. (c) Mg||Mg cells cycled at a current density of 2 mA cm^{-2} to a cutoff capacity of 2 mAh cm^{-2} using the different electrolytes. Raman spectra of G2 and G2-FDOL electrolytes in (d) 780 – 920 cm^{-1} and (e) 720 – 780 cm^{-1} regions. (f) RDFs (solid lines; left axis) and coordination numbers (dashed lines; right axis) of Mg-O (G2) interactions in both G2 and G2-FDOL electrolytes.

found that 0.4 M gives high ionic conductivity, low overpotential, and stable Mg cycling [39]. Coulombic efficiency (CE) was first evaluated in Mg||Pt cells to determine the optimal volume percentage of FDOL in a 0.4 M $Mg[Al(hfip)_4]_2$ in G2 electrolyte. The addition of 10 vol.% FDOL to the base electrolyte improved cycling stability, and the CE has increased from 98.5 to 99.2% (Figure 1). The electrolytes showed similar overpotentials (45 vs 47 mV) and ionic conductivity (6.0 vs 5.7 mS cm^{-1}, Note S2 and Figure S3). Further increase in the volume percentage of FDOL resulted in a decrease in CE (Figure 1a; Figure S4) and ionic conductivity (Figure S3), accompanied by an increase in overpotentials (Figure 1a; Figure S4). Electrolytes with 25 – 75 vol.% FDOL also experienced short-circuiting during the early stages of Mg plating/stripping (see Figure 1b; Figure S5), indicating that higher FDOL contents worsen the Mg metal performance. The 0.4 M $Mg[Al(hfip)_4]_2$ in G2 also suffered from "soft" internal short circuits. For instance, at the 70th Mg plating/stripping cycle, this electrolyte exhibited voltage fluctuations (Figure S6), despite maintaining comparable CE. These soft shorts were transient and reversible, did not lead to cell failure, and occurred only after prolonged cycling or under higher current densities. Importantly, all CE values and overpotential comparisons in Figure 1a were derived from the macrocycling tests (Figure S4) and from the 5th Mg plating/stripping cycle (Figure S5), during which both electrolytes exhibited stable voltage profiles with no fluctuations attributable to soft shorting. Thus, the improved performance of the G2-FDOL electrolyte is not exaggerated by baseline (G2) electrolyte failure but rather indicates a true improvement in Mg plating/stripping. In continuation, we will therefore focus on two electrolytes: 0.4 M $Mg[Al(hfip)_4]_2$ in G2 and 0.4 M $Mg[Al(hfip)_4]_2$ in G2 with 10 vol.% FDOL, hereinafter referred to as G2 and G2-FDOL electrolytes, respectively. While both electrolytes exhibited similar stability in Mg||Mg cells for approximately 200 h at a low current density of 0.1 mA cm^{-2} (Figure S7a), significant differences emerged at higher current densities (1 mA cm^{-2}, Figure S7b and 2 mA cm^{-2}, Figure 1c).

We additionally evaluated other commonly used fluorinated ethers in battery electrolytes, including bis(2,2,2-trifluoroethyl) ether (BTFE) [29, 40] and 1,1,2,2-tetrafluoroethyl-2,2,3,3-tetrafluoropropyl ether (TTE) [29, 41], in $Mg[Al(hfip)_4]_2$-based electrolytes (Figure S8a–e). We also investigated a series of

16146840, 2026, 18, Downloaded from https://advanced.onlinelibrary.wiley.com/doi/10.1002/aenm.202506415 by Ervin Rems - Bibliothèque de Sorbonne Université , Wiley Online Library on [15/05/2026]. See the Terms and Conditions (https://onlinelibrary.wiley.com/terms-and-conditions) on Wiley Online Library for rules of use; OA articles are governed by the applicable Creative Commons License

other dioxolane-based cyclic ethers: 1,3-dioxolane (DOL, non-fluorinated; Figure S8f), 2-(trifluoromethyl)dioxolane (TFDOL, containing one $-CF_3$ group on C—O—C; Figure S8f), and FDOL (containing two $-CF_3$ groups on C—O—C; Figure S8f). The FDOL-based electrolyte clearly outperformed those containing BTFE, TTE, DOL, or TFDOL, highlighting the potential of FDOL in $Mg[Al(hfip)_4]_2$-based Mg electrolytes for improved Mg anode operation (see Figure S8 and Note S3). We further examined the effect of FDOL in other Mg electrolytes containing $Mg(TFSI)_2$ [42], $MgCl_2$, [43, 44], magnesium trifluoromethanesulfonate ($Mg(OTf)_2$) [45], and magnesium fluorinated alkoxyborate salt ($Mg[B(hfip)_4]_2$) [25] salts. As discussed in Note S3 and shown in Figure S9a–g, introducing 10 vol.% FDOL into $Mg(TFSI)_2$-, $Mg(OTf)_2$-, and $MgCl_2$-based electrolytes does not improve the Mg metal performance. In contrast, FDOL addition increases the CE of Mg plating/stripping in the $Mg[B(hfip)_4]_2$/G2 electrolyte (Figure S9h–k), indicating that the positive effect of FDOL seems to be specific to electrolytes containing weakly coordinating, bulky anions such as $[B(hfip)_4]^-$ and $[Al(hfip)_4]^-$. Specifically, Mg metal performance is best in $Mg[Al(hfip)_4]_2$/G2-FDOL electrolyte, as evidenced by lower overpotentials and higher CE stability for Mg plating/stripping (Figure 1b vs Figure S9k). This observation is consistent with the generally poor baseline performance of $Mg[B(hfip)_4]_2$-based electrolytes relative to their $Mg[Al(hfip)_4]_2$-based electrolytes [26, 27]. Accordingly, we focused our investigations on the $Mg[Al(hfip)_4]_2$-based electrolytes.

To investigate this, we employed Raman spectroscopy to study the effect of FDOL addition to the Mg electrolytes. The Raman spectra in the 720 – 920 cm^{-1} range for different Mg salts and solvents are shown in Figure S10. Based on previous studies, the Raman spectra of Mg electrolytes can be divided into two key regions: the 780–920 cm^{-1} range, which is particularly informative for identifying different solvent conformers [46], and the 720–780 cm^{-1} range, typically associated with anion-related interactions [47]. Within the 780 – 920 cm^{-1} spectral region (Figure 1d; Figure S11a–c), characteristic bands corresponding to glyme conformers are observed. These vibrations, primarily arising from C—O stretching and $-CH_3$ modes, are highly sensitive to molecular conformation and solvent-ion coordination. The Raman band near 885 cm^{-1} has been consistently assigned to Mg^{2+}-coordinated glyme species in Mg-glyme systems [29, 48] arising from coordination-sensitive C—O and C—H related modes. Although this region includes contributions from several C—O stretching and C—H bending vibrations, prior studies show that these non-coordinated modes do not exhibit systematic intensity changes upon modification of Mg^{2+} solvation. In contrast, the ~885 cm^{-1} band increases specifically when G2 participates in Mg^{2+} solvation based on the recent studies [29]. Upon addition of 10 vol.% FDOL to the 0.4 M $Mg[Al(hfip)_4]_2$ in G2 electrolyte, the intensity of the free G2 band (cca. 810 cm^{-1}) decreases, while the free FDOL peak (800 cm^{-1}) appears. Similar behavior is observed in other Mg electrolytes (Figure S11a–c). Concurrently, the band corresponding to coordinated G2 (Mg^{2+}-G2, approx. 885 cm^{-1}) increases slightly. These results indicate that the incorporation of FDOL potentially enhances Mg^{2+}-G2 coordination, thereby reducing the fraction of free G2 molecules in the electrolyte. This behavior is consistent with observations reported in previous studies [29].

The $[Al(hfip)_4]^-$ anion peak at ~762 cm^{-1} remains unchanged in position and intensity upon addition of 10 vol.% FDOL to 0.4 M $Mg[Al(hfip)_4]_2$ in G2, indicating that no contact ion pairs (CIPs) are formed in the FDOL-G2 electrolyte (Figure 1e). In contrast, the addition of FDOL to $Mg(TFSI)_2$, $MgCl_2$, and $Mg(OTf)_2$-based electrolytes (Figure S11d–f) promotes CIP formation, as evidenced by blue shifts of the TFSI anion peak at ~740 cm^{-1}, yielding monodentate CIPs (mono-CIPs, ~743 cm^{-1}) and bidentate CIPs (bi-CIPs, ~749 cm^{-1}) [29]. This could explain why FDOL addition does not improve Mg metal performance in these electrolytes (see Figure S9), as a large fraction of CIPs is reduced during Mg plating [31, 42]. Raman results suggest that in $Mg[Al(hfip)_4]_2$-based electrolytes, FDOL addition effectively reduces free G2, Mg^{2+}-FDOL, and Mg^{2+}-anion coordination, stabilizing the Mg^{2+} solvation environment. We also found consistent results using the Fourier transform infrared spectroscopy (FTIR) as described in Note S4 and Figure S12.

To further validate these findings, molecular dynamics (MD) simulations were conducted to examine the radial distribution functions (RDFs) and coordination numbers for Mg—O and Mg—F interactions with the $[Al(hfip)_4]^-$ anion, FDOL, and G2. In all electrolytes, the primary coordination shell of Mg^{2+} is dominated by oxygen atoms from G2 (Figure 1f). This agrees with the bidentate coordination of G2, where both terminal ether oxygens contribute to Mg^{2+} solvation, and is consistent with the Raman results in Figure 1e, which show increased bonded G2 intensity in the FDOL-based electrolyte. The $[Al(hfip)_4]^-$ anion does not participate in the first solvation shell of Mg^{2+}; Mg—O (anion) and Mg—F (anion) RDFs display only broad features beyond 5 Å, confirming its weakly coordinating nature (Figure S13a,b). Mg^{2+}-FDOL interactions are negligible, as no distinct Mg—O or Mg—F peaks from FDOL appear within the first coordination shell. Although FDOL contains oxygen atoms, steric hindrance from its cyclic structure restricts its approach to Mg^{2+}, preventing first-shell coordination. This is reflected by the broader, weaker Mg—O and Mg—F (FDOL) RDF peaks and coordination numbers below 1 across all compositions (Figure S13c), consistent with the Raman data. This is further supported by an additional MD simulation of G2-free electrolyte (where FDOL is mainly used as a solvent), as shown in Figure S13d,e, where Mg—O RDFs involving FDOL show only weak, low-intensity features, and coordination numbers well below one. Thus, FDOL interacts with Mg^{2+} predominantly through weak, outer-shell, packing-driven proximity rather than through chemically meaningful coordination.

We also calculated the diffusion coefficients (D_i) of the G2 and G2-FDOL electrolytes and found that the G2-FDOL electrolyte displays the lowest D_i, even below neat G2 (Figure S14a), indicating a more dynamically constrained medium in this electrolyte. This further validates that the increased Mg^{2+}-G2 coordination in G2-FDOL electrolyte, which is consistent with Raman and MD simulation results. The intermittent residence correlation function, τ_{int}, was computed specifically for Mg—O(G2) contacts to measure persistence of Mg^{2+}-G2 coordination in these electrolytes, given that Mg—O (FDOL) is virtually non-coordinating. G2-FDOL electrolyte exhibits the largest τ_{int}, indicating the most persistent Mg^{2+}-G2 contacts in the first coordination shell (Figure S14b). However, the decay of $C(t)$ in both of these electrolytes is similar (Figure S14c). These results demonstrate that FDOL

16146840, 2026, 18, Downloaded from https://advanced.onlinelibrary.wiley.com/doi/10.1002/aenm.202506415 by Ervin Rems - Bibliotheque de Sorbonne Universite , Wiley Online Library on [15/05/2026]. See the Terms and Conditions (https://onlinelibrary.wiley.com/terms-and-conditions) on Wiley Online Library for rules of use; OA articles are governed by the applicable Creative Commons License

does not directly coordinate Mg^{2+}, but instead modulates the coordination-shell occupancy and exchange dynamics of G2 indirectly, likely by altering anion-solvent packing competition.

In essence, the addition of 10 vol.% FDOL to $Mg[Al(hfip)_4]_2$-based electrolytes improves the Mg^{2+} solvation structure by minimizing free G2 and CIP formation while enhancing Mg^{2+}-G2 coordination, consistent with the efficient Mg^{2+} solvation strategy employing fluorinated ethers in Mg electrolytes as proposed by Hahn et al. [29] Importantly, we believe that varying both salt concentration and FDOL content simultaneously would give more information but also complicate mechanistic interpretation, as salt concentration alone strongly influences CIP formation, viscosity, and passive layer formation on the Mg metal anode, and therefore will be conducted in future work.

Based on the improved Mg metal performance of G2-FDOL electrolytes, we tested the oxidative stability of these electrolytes by linear sweep voltammetry (LSV). G2-FDOL electrolyte showed higher oxidative stability (4.1 V at 0.5 mV s^{-1}, Figure 2a), which is corroborated by the lower highest occupied molecular orbitals (HOMO) energy levels of FDOL solvent (Figure S15a). The Mg^{2+}-solvent pairs also reveal that FDOL has a more negative HOMO than G2 (−17.28 eV vs −15.39 eV), indicating that FDOL is intrinsically harder to oxidize and experiences weaker frontier orbital destabilization upon Mg^{2+} contact (Figure S15b,c). Improved oxidative stability was further validated under slow scan rates (Figure S16a) and with the use of a carbon-coated Al electrode (Figure S16b).

To benchmark this in full cell operation, we selected a commercially available high-voltage organic cathode, polyaniline (PANI). Recent work by Li et al. [31, 49] investigated the use of $Mg(TFSI)_2$/DME electrolyte in Mg||PANI cells at a high voltage of 3.5 V. Building on this study, we demonstrate that Mg||PANI cells utilizing the G2-FDOL electrolyte could be cycled up to a high cut-off voltage of 3.5 V, delivering a specific discharge capacity of 200 mAh g^{-1} at 0.1 C (1C = 250 mA g^{-1}). In contrast, Mg||PANI cells cycled in the G2 electrolyte exhibited a lower specific capacity of 118 mAh g^{-1} at 0.1 C with poor rate capability (Figure 2b,c) with reduced and unstable CEs (Figure S17). Conversely, PANI in the G2-FDOL electrolyte exhibited good rate capability, delivering specific discharge capacities of 149, 112, and 82 mAh g^{-1} at 0.5, 1, and 2 C, respectively (Figure 2b,d), with relatively higher and stable CEs (Figure S17). We performed additional galvanostatic charge–discharge measurements using electrodes composed solely of carbon black and binder in the same 3:1 ratio used for the composite organic cathode, tested under identical conditions to the Mg||PANI cells. As shown in Figure S18, both electrolytes exhibit a certain degree of irreversibility at higher potentials under low-current conditions. This behavior is expected, as oxidative stability values obtained from LSV on planar Pt electrodes are known to overestimate practical stability. When applied to high-surface-area composite electrodes, these limitations become more pronounced, resulting in partial electrolyte decomposition at elevated potentials. For the G2-FDOL electrolyte, the capacitive contribution was subtracted from the total capacity measured in the half-cell configuration, with the corrected values summarized in Table S1. The PANI electrode exhibits incomplete capacity utilization, reaching approximately 70% at 0.1C, which is consistent with previously reported results obtained within the same voltage window. Finally, the long-term cycling stability at 1 C after the rate capability test in both electrolytes showed retained discharge capacity in G2-FDOL electrolyte (86 mAh g^{-1} or 76% after 500 cycles at 1 C, Figure 2e; Figure S19b). In contrast, the G2 electrolyte exhibited significantly lower performance, retaining only 10 mAh g^{-1} after 30 cycles (Figure S19a).

We further extended our investigation to three chemically distinct cathodes: the Chevrel-phase intercalation cathode Mo_6S_8, a sulfur conversion cathode, and the organic cathode poly(hydroquinonyl-benzoquinonyl sulfide) (PHBQS [50]). Their electrochemical performance in the FDOL-containing electrolyte was systematically compared with that in the baseline G2 electrolyte. In Mg||Mo_6S_8 cells, both electrolytes exhibited comparable performance at a low rate of 0.1C (Figure S20a,b,e). However, at a higher rate of 1 C, pronounced differences emerged (Figure S20c–e) with G2-FDOL outperforming G2. The G2-FDOL electrolyte also demonstrated improved performance in Mg||S cells (Figure S21), while even more distinct differences were observed in Mg||PHBQS cells (Figure S22). When the Mg||PHBQS cells were cycled up to 3 V, the G2-FDOL electrolyte clearly outperformed the G2 electrolyte, in agreement with trends observed for Mg||PANI cells. Taken together, these results, along with symmetric Mg performance data displayed in Figure 1 showing improved performance under high current densities, indicate that the advantages of the G2-FDOL electrolyte manifest predominantly under high-voltage or otherwise demanding operating conditions. This highlights the potential of the G2-FDOL formulation for enabling high-voltage RMBs.

Three-electrode measurements were performed to electrochemically separate the overpotential contributions of the Mg anode (E_{Mg}) and the PANI cathode (E_{PANI}) in Mg||PANI cells, where the full-cell voltage corresponds to ($E_{PANI} - E_{Mg}$). This configuration enables direct evaluation of the electrochemical behavior of both electrodes. The first five cycles and the corresponding E_{Mg}, E_{PANI}, and ($E_{PANI} - E_{Mg}$) values in G2 and G2-FDOL electrolytes are presented in Figure 2f,g. Note that due to the pseudo-nature of the reference, its potential is not stable for the full duration of the experiment, which is visible at approx. 0.6 h, 1.3 h, and 3.1 h in the G2-FDOL experiment (Figure 2g). At those points, the potential of both electrodes was suddenly shifted in the same direction, while the $E_{PANI} - E_{Mg}$ does not show any shifts, which suggests a change in the pseudo-reference potential. In addition, the experiment reveals a significant difference between the two electrolytes regarding the relative contributions of PANI and Mg to the internal resistance. Because the reference electrode was unstable during the first two cycles, which distorts the values and complicates the analysis, we will employ the data from the fifth cycle.

The cells were discharged over a voltage range of 3.5 to 0.5 V. Of the 3 V range, the PANI cathode accounted for 1.75 V (58% of losses) in the G2 electrolyte and 2.63 V (88% of losses) in the G2-FDOL electrolyte. Conversely, the Mg electrode accounted for 1.25 V in G2 (42%) and 0.37 V in G2-FDOL (12%). From this division alone, it is evident that the Mg anode contributes a larger share of the internal losses for G2 electrolyte than in G2-FDOL electrolyte. Although the PANI electrode in G2 technically contributes the majority (58%), these losses account

16146840, 2026, 18, Downloaded from https://advanced.onlinelibrary.wiley.com/doi/10.1002/aenm.202506415 by Ervin Rems - Bibliothèque de Sorbonne Université , Wiley Online Library on [15/05/2026]. See the Terms and Conditions (https://onlinelibrary.wiley.com/terms-and-conditions) on Wiley Online Library for rules of use; OA articles are governed by the applicable Creative Commons License

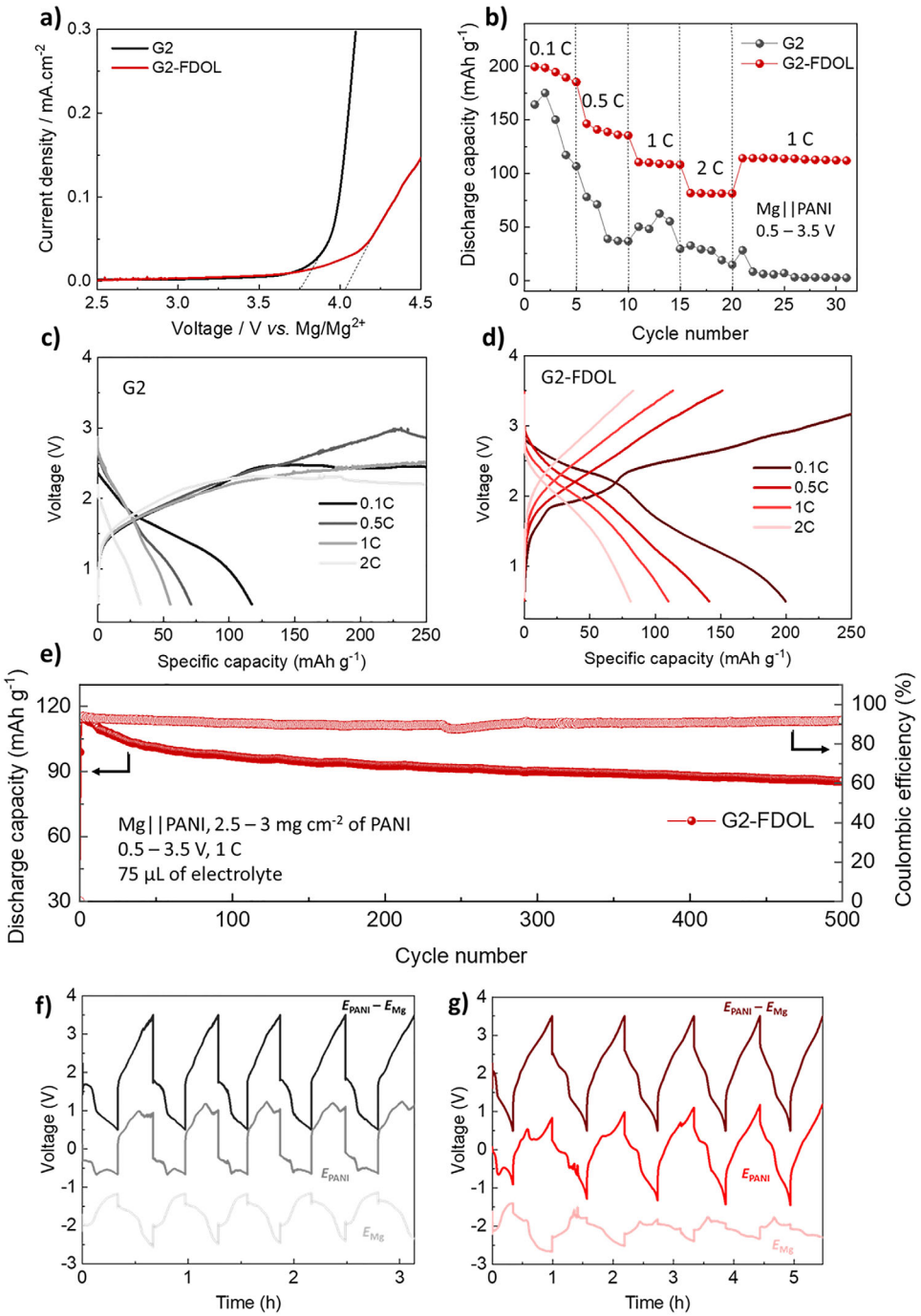

FIGURE 2 | (a) Oxidative LSV of different electrolytes in Mg||Pt cells at 0.5 mV s^{-1}. (b) Rate capability in terms of discharge capacity of Mg||PANI cells cycled in different electrolytes. Charge–discharge voltage profiles (at 2nd cycle) of Mg||PANI cells cycled at different charge/discharge rates using: (c) G2 and (d) G2-FDOL electrolytes. (e) Long-term cycling performance of Mg||PANI cells at 1 C following the rate capability test in studied electrolytes. Voltage profiles and separated electrode potentials recorded during the first five discharge/charge cycles in (f) G2 and (g) G2-FDOL electrolytes in three-electrode Mg||Au||PANI cells.

for the initial activation at the beginning of either charge or discharge. The end of discharge or charge, on the other hand, is controlled by the Mg anode. To explain, at a low state of charge, the PANI electrode exhibits a plateau, while the Mg electrode shows an increase in overpotential, bringing the electrodes to the set limit of $E_{PANI} - E_{Mg}$ of 0.5 V and stopping the discharge. A similar situation occurs during charging: the PANI electrode first overshoots the final end potential and begins to show small voltage fluctuations (which could be erroneously attributed to soft short circuits from 2E experiments alone), while the potential of the Mg anode suddenly decreases and ends the charge. Contrary to that, in G2-FDOL electrolyte, the Mg electrode is significantly more stable and shows plateaus both at the end of discharge and at the end of charge, while the PANI electrode overpotential increases both at high SOC and low SOC, controlling the overall performance. There is therefore a large difference in which

16146840, 2026, 18, Downloaded from https://advanced.onlinelibrary.wiley.com/doi/10.1002/aenm.202506415 by Ervin Rems - Bibliothèque de Sorbonne Université , Wiley Online Library on [15/05/2026]. See the Terms and Conditions (https://onlinelibrary.wiley.com/terms-and-conditions) on Wiley Online Library for rules of use; OA articles are governed by the applicable Creative Commons License

electrode controls the Mg||PANI performance, which is the PANI cathode in G2-FDOL electrolyte, while for G2 electrolyte, both electrodes contribute roughly half. If we look at relative changes from switching from G2 to G2-FDOL electrolyte, it is important to note that the overall contribution of Mg internal losses is almost quartered when switching from G2 to G2-FDOL electrolyte (42% to 12%).

To check the operation of both PANI and Mg electrodes independently, we performed parallel SEM imaging on PANI and Mg electrodes cycled in G2 and G2-FDOL electrolytes, examined at both fully charged (3.5 V) and fully discharged (0.5 V) states (Figure S23). In terms of the morphology of PANI, no discernible differences are observed between the two electrolytes. In both cases, the electrodes exhibit a similar microstructure, characterized by polymeric particles embedded in a matrix of carbon black and PTFE fibers, with no visible evidence of surface layer formation induced by electrochemical cycling. Complementary energy-dispersive X-ray spectroscopy (EDS) analysis was also performed on the same electrodes (Table S2), which reveals an increased fluorine content in the charged state, indicating predominant coordination with an anionic species, most likely Alhfip$^-$. This observation is consistent with previous reports in the literature [31, 51]. Importantly, no significant differences in elemental composition are detected between electrodes cycled in G2 and G2-FDOL electrolytes. Importantly, most elements observed in the EDS analysis showed similar contents between G2 and G2-FDOL samples of charged PANI electrodes. The element showing a statistically relevant change was fluorine, which could be either due to: (i) difference in local PTFE content (variation of fluorine content on 10 different PANI pristine cathodes was found to be between 4.9 and 5.6%), (ii) natural inconsistencies between samples (only one cathode was examined for both G2 and G2-FDOL analysis) or (iii) formation of a more fluorine-poor CEI on the cathode surface. The latter possibility would fit with the observed differences on cycled Mg anodes, but we found no definitive proof in the literature that PANI cathodes form a CEI layer, and we also did not detect any Mg in the sample, which should also be present in the CEI, so we deem the analysis inconclusive. For Mg metal anode, on the other hand, there is a distinct difference in the morphology of the electrodes, with the Mg cycled in G2 showing significantly less uniform surface activation than the electrode from G2-FDOL (Figure S23), which is in line with the differences in voltage losses observed with the 3E experiment (Figure 2f,g).

Due to the organic nature of PANI and its partial solubility in ether-based electrolytes, it is known that the dissolved cathode species can migrate toward the Mg metal anode, where they may aggravate interfacial instability and also facilitate micro-shorting [52, 53]. To assess this possibility, we investigated the solubility of the cycled PANI cathode by soaking PANI electrodes in the G2 and G2-FDOL electrolytes for 24 h. As shown in Figure S24a, no visible dissolution of the PANI electrode is observed in either of the electrolytes. UV–vis spectroscopy was employed to further confirm the absence of dissolved species (Figure S24b). As a reference, the PANI electrode was also soaked in LP40 (1 M $LiPF_6$ in EC/DEC (1/1 vol.%)), as PANI is expected to exhibit higher solubility in highly protic solvents, such as ethylene carbonate [1], which was indeed seen in Figure S24a. Depending on the doping state, PANI should exhibit an absorption band between 630–650 nm (exciton band) in the emeraldine base form, or a broad, delocalized conduction band between 750 and 850 nm, in the emeraldine salt form, with the exact position depending on the solvent and doping level [2]. In the LP40 electrolyte, in which PANI is soluble, a broad band is observed, with the absorption maximum at around 790 nm. In contrast, no absorption bands were detected in either G2 or G2-FDOL, for electrodes in either the charged or discharged state, confirming that PANI does not have significant solubility in the employed Mg electrolytes (Figure S24b).

To further isolate the influence of the electrolyte on the PANI electrode, independent of the Mg metal anode, we conducted symmetric cell measurements using one pre-cycled and one pristine PANI electrode, following a previously reported methodology from our group [54]. As shown in Figure S24c,d, the electrochemical behavior in both electrolytes is comparable, with a slightly higher overpotential observed for the G2-FDOL electrolyte. This difference can be attributed to its lower ionic conductivity as observed in Figure S3. None of the tests therefore showed a definitive answer as to why the PANI electrode has a larger overpotential in the beginning of discharge or charge in G2 electrolyte. Solubility in both electrolytes seemed to be below the level of detection in both electrolytes, and symmetrical PANI cells worked better in G2 than in G2-FDOL. Although we expected a difference in full cell performance due to the higher oxidative stability of the G2-FDOL electrolyte, the results show that the difference in performance is likely attributed to the instability of the Mg anode in the G2 electrolyte, with significant differences in voltage loss contributions of the Mg anode supported with SEM micrographs showing morphological differences in the uniformity of the anode activation. Consequently, the improved performance observed in full Mg||PANI cells employing the G2-FDOL electrolyte can be primarily ascribed to improvements at the Mg metal anode interface rather than to changes in the PANI electrode itself. Hence, we focused our further investigations on the underlying mechanisms responsible for the improved electrochemical performance of Mg metal in the G2-FDOL electrolyte.

Initially, we attempted to determine the Mg metal anode mechanism of operation by measuring EIS at open circuit voltage (OCV) conditions. This gives limited information on the electrochemical processes happening on the Mg metal anode during operation due to passive layer growth (Figure 3e; Figure S25 and Note S5). Therefore, we employed *operando* EIS to obtain insights into the transport and reaction processes on the Mg metallic anode. This technique allows for real-time monitoring of cell impedance by recording EIS spectra during cycling and has been applied to Mg metal anode studies in the past [14, 50, 55]. The key advantage of *operando* EIS is that it eliminates the need for an equilibration period before the measurement, which is required in conventional EIS performed at OCV. This equilibration period can introduce significant changes in the cell due to side reactions, such as the formation of a passive layer on the Mg metal surface, potentially obscuring the true electrode dynamics. Based on this, we conducted *operando* EIS measurements in Mg||Mg two-electrode (2E) cells during the first half cycle of Mg plating/stripping for G2 and G2-FDOL (Figure 3a,c). As illustrated, *operando* EIS reveals a significantly lower impedance, on the order of 30 – 100 Ω. Additionally, distinct

16146840, 2026, 18, Downloaded from https://advanced.onlinelibrary.wiley.com/doi/10.1002/aenm.202506415 by Ervin Rems - Bibliothèque de Sorbonne Université , Wiley Online Library on [15/05/2026]. See the Terms and Conditions (https://onlinelibrary.wiley.com/terms-and-conditions) on Wiley Online Library for rules of use; OA articles are governed by the applicable Creative Commons License

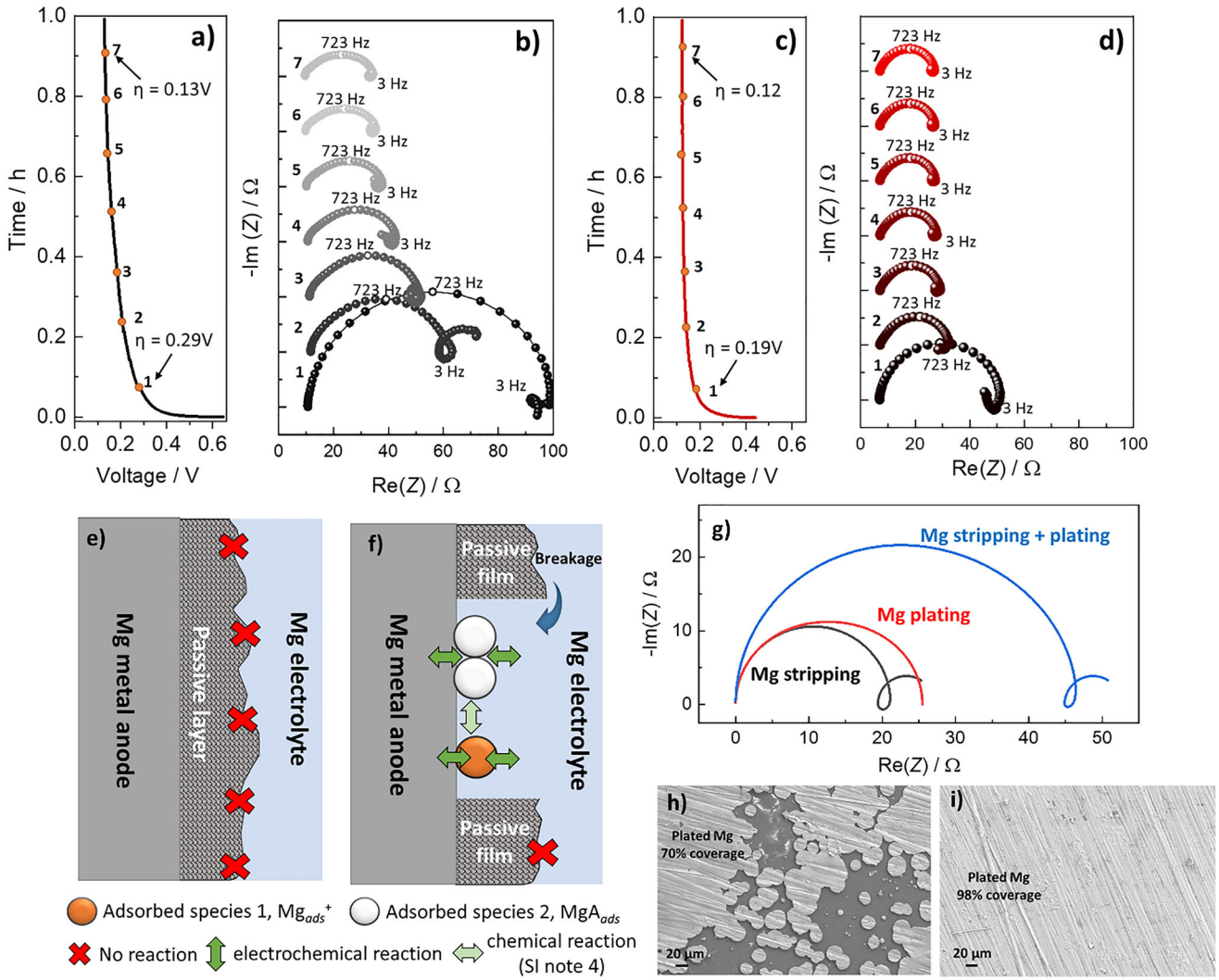

FIGURE 3 | Voltage profiles of the first half cycle for Mg||Mg 2E cells cycled at a current density of 2 mA cm^{-2} to a cutoff capacity of 2 mAh cm^{-2} in (a) G2 and (c) G2-FDOL electrolytes. The corresponding *operando* EIS spectra for Mg||Mg 2E cells cycled in (b) G2 and (d) G2-FDOL electrolytes. Schematic illustration of electrochemical processes happening on Mg metallic anode under (e) OCV and (f) bias conditions. (g) Simulated EIS spectra for oxidized Mg electrode (stripping, black line), reduced Mg electrode (plating, red line), and for the complete cell (Mg stripping + plating, blue line). The current flowing through the cell equals 2 mA, and the surface area is assumed to be equal to the geometric surface area (1 cm^2). The absolute overvoltage on both electrodes is 150 mV. The values of all model parameters are given in Note S9. SEM images of Mg deposits on Celgard separator extracted from Mg||Mg cells cycled for the first half cycle in (h) G2, (i) G2-FDOL electrolytes. All the Mg electrodes used here were 12 mm in diameter.

features are identified, including a prominent high-frequency arc (723 Hz) and inductive loops at low frequencies (3 Hz) (Figure 3b,d).

Preliminary simulations of different possible multistage reaction scenarios have shown that the present experimental results can be reproduced with different mechanisms consisting of chemical or electrochemical elementary steps as schematically illustrated in Figure 3f. In all cases, however, two different adsorbed intermediates must be present on the magnesium surface. In the following example, we assume that the two adsorbed species are Mg^{+}_{ads} and Mg_{ads} and that the overall mechanism consists of the following 4 steps (another possible scenario is explained in Note S6):

$$\mathrm{Mg} \underset{k_2}{\overset{k_1}{\rightleftarrows}} \mathrm{Mg}^{+}_{ads} + \mathrm{e}^{-} \tag{1}$$

$$\mathrm{Mg}^{+}_{ads} \underset{k_4}{\overset{k_3}{\rightleftarrows}} \mathrm{Mg}^{2+} + \mathrm{e}^{-} \tag{2}$$

$$\mathrm{Mg} + \mathrm{A}^{-} \underset{k_6}{\overset{k_5}{\rightleftarrows}} \mathrm{MgA}_{ads} + \mathrm{e}^{-} \tag{3}$$

$$\mathrm{MgA}_{ads} \underset{k_8}{\overset{k_7}{\rightleftarrows}} \mathrm{Mg}^{2+} + \mathrm{e}^{-} + \mathrm{A}^{-} \tag{4}$$

16146840, 2026, 18, Downloaded from https://advanced.onlinelibrary.wiley.com/doi/10.1002/aenm.202506415 by Ervin Rems - Bibliothèque de Sorbonne Université , Wiley Online Library on [15/05/2026]. See the Terms and Conditions (https://onlinelibrary.wiley.com/terms-and-conditions) on Wiley Online Library for rules of use; OA articles are governed by the applicable Creative Commons License

Although the presence of species A (here assumed as being an anion in the electrolyte phase) is strongly suggested from the impedance analysis, unfortunately, its chemical nature cannot be easily established. Still, for the present purposes, such a general model can be useful for the determination of several mechanistic processes that occur on the surface of magnesium before and during cycling (stripping and plating).

Figure 3g shows a simulated EIS spectrum based on Equation (S11) shown and derived in Notes S7–S9 and Figure S26, with the rate constants adjusted so that the spectrum resembles the typical measured shape in Figure 3b. Using a quantitative model, we were therefore able to capture the measured impedance features and attribute them to a multi-step charge transfer reaction process, which involves at least four redox reactions and two different adsorbed species. It should be noted that from the measurement we can obtain only the approximate shape for the whole cell, that is, the shape of the graph referred to as "stripping + plating". The deconvolution into two separate contributions of the two electrodes is not unique, that is, different shapes and sizes could be generated for the individual electrodes if reliable 3E measurements are not available. However, given the current state of understanding of the mechanisms operating at Mg metallic electrodes, we find it remarkable that both the shape and the magnitude of the typical *operando* impedance spectrum (in the wide range from 100 kHz to 20 mHz) can be explained by the reaction mechanism alone. In other words, to explain the typical spectra shown in Figure 3b,d, no transport restrictions due to migration through the passive layer or diffusion processes in pores/cracks, etc., need to be considered. This is a stark contrast to lithium electrodes, where the transport through the passive film (solid electrolyte interface) is a decisive factor determining the electrode dynamics [33, 56].

Initial *operando* EIS spectra show smaller charge transfer resistances for G2-FDOL electrolyte (50 Ω vs 100 Ω for G2, Figure 3b,d). The values progressively decrease with cycling time to 25 Ω and 35 Ω (G2-FDOL and G2, respectively). The change in EIS values follows the change in overpotentials – distinct differences are observed at the beginning of cycling, while both electrolytes exhibit similar values by the end of the first half cycle. Ex situ analysis of the electrodes after the first half cycle of stripping and plating showed pits on the stripped electrode surface, while it wasn't possible to straightforwardly visualize the Mg deposits on the plated electrode, since they grew into the separator pores and detached together with the separator from the electrode (Figure S27a; Figure S28). The electrode, from which the deposits were detached, showed a flat, brushed surface close to identical to a pristine brushed Mg electrode (Figures S2b–S27d). The degree of active electrode surface area was higher for the G2-FDOL electrolyte, which is shown both through a difference in % of coverage (98 vs 70%, determined from the surface area of plated Mg on the separator, Figure 3h,i) and a more homogeneous distribution of pits on the stripped electrode surface (Figure S27e,f, which is in accordance to the morphology of the cycled Mg electrodes extracted from Mg||PANI cells). We attribute this to the direct cause of the difference in the initial overpotential and charge transfer reaction resistance values. The larger active surface area of the electrode results in a smaller charge transfer resistance.

The overpotential and resistance decrease during the half-cycle experiment could be due to (i) a further gradual increase in the active surface area of the stripped electrode (more breakage of the passive layer) or (ii) high surface area deposits increasing the active surface area on the other electrode. *Operando* EIS already gives an indication that the high surface area deposition is happening, since the EIS arc shape changes with progressive stripping/plating to produce a 45° angle at the high frequency of the arc (see Figure 3b). Furthermore, high surface area deposits are supported by the entanglement of the deposits inside the porous separator as evidenced by the ex situ analysis, so we attribute this effect to stem mostly from the electrode undergoing deposition. This hypothesis was tested using three-electrode (3E) Mg||Au||Mg cells (Figure S29), from which we determined that the initial drop in overpotential (approx. 0.05 h) happens due to the electrode undergoing stripping where the electrode is activated through the breakage of the passive layer, while subsequent gradual decrease corresponds to the electrode undergoing plating, the effect stemming from high surface area deposition increasing the active surface area of the electrode. The effect is more prominent in the G2 electrolyte (larger impedance decrease, Figure 3b, and larger counter electrode overpotential decrease, Figure S29), which suggests a higher degree of high surface area deposition in this electrolyte. G2-FDOL electrolyte, on the other hand, showed more uniform deposition.

This phenomenon can be explained with the present model, as shown in Note S10 and Figure S30 and briefly summarized in the continuation. From Equation (S7) we can see that the current caused by the surface reaction depends only on the electrode surface (A_{geom}) and the rate constants for all elementary steps. The microscopy results (Figure 3h,i) strongly indicate that the electrode surface changes significantly during the galvanostatic experiment. In particular, we estimate that the surface area of the electrode that is plated increases for approx. 27x (from 1 to 27 cm^2). As the current is kept constant, the change in the electrode surface can only be adjusted by a corresponding reduction in the rate constant(s), which may involve a corresponding reduction in the overvoltage. For similar reasons, an increase in surface area can lead to a reduction in the size of the main impedance arc due to the plating reaction. Both phenomena are quantitatively demonstrated using the present model in Figure S31a,b. Although these calculations are only approximate (due to the lack of accurate values for the many kinetic parameters), the ability to explain the main experimental trends during the *operando* impedance experiment confirms the kinetic origin of the main measured impedance contributions.

EIS analysis of the G2-FDOL electrolyte, therefore, showed a similar mechanism of operation to the electrolyte without fluorinated ether, while the performance was improved through more uniform activation of the electrode surface area and deposition (i.e., a decrease in surface area of the deposits). To test whether long-term stability also originates from the same effects, we continued the investigation by measuring *operando* EIS at the 10th cycle of Mg plating/stripping. According to the understanding of the plating and stripping behavior of metal electrodes [56, 57], we expect that the electrode's morphology is significantly different after the 10th cycle of the experiment. Although we started from planar electrodes, uneven stripping and high surface area deposition likely produced porous structures

16146840, 2026, 18, Downloaded from https://advanced.onlinelibrary.wiley.com/doi/10.1002/aenm.202506415 by Ervin Rems - Bibliotheque de Sorbonne Universite , Wiley Online Library on [15/05/2026]. See the Terms and Conditions (https://onlinelibrary.wiley.com/terms-and-conditions) on Wiley Online Library for rules of use; OA articles are governed by the applicable Creative Commons License

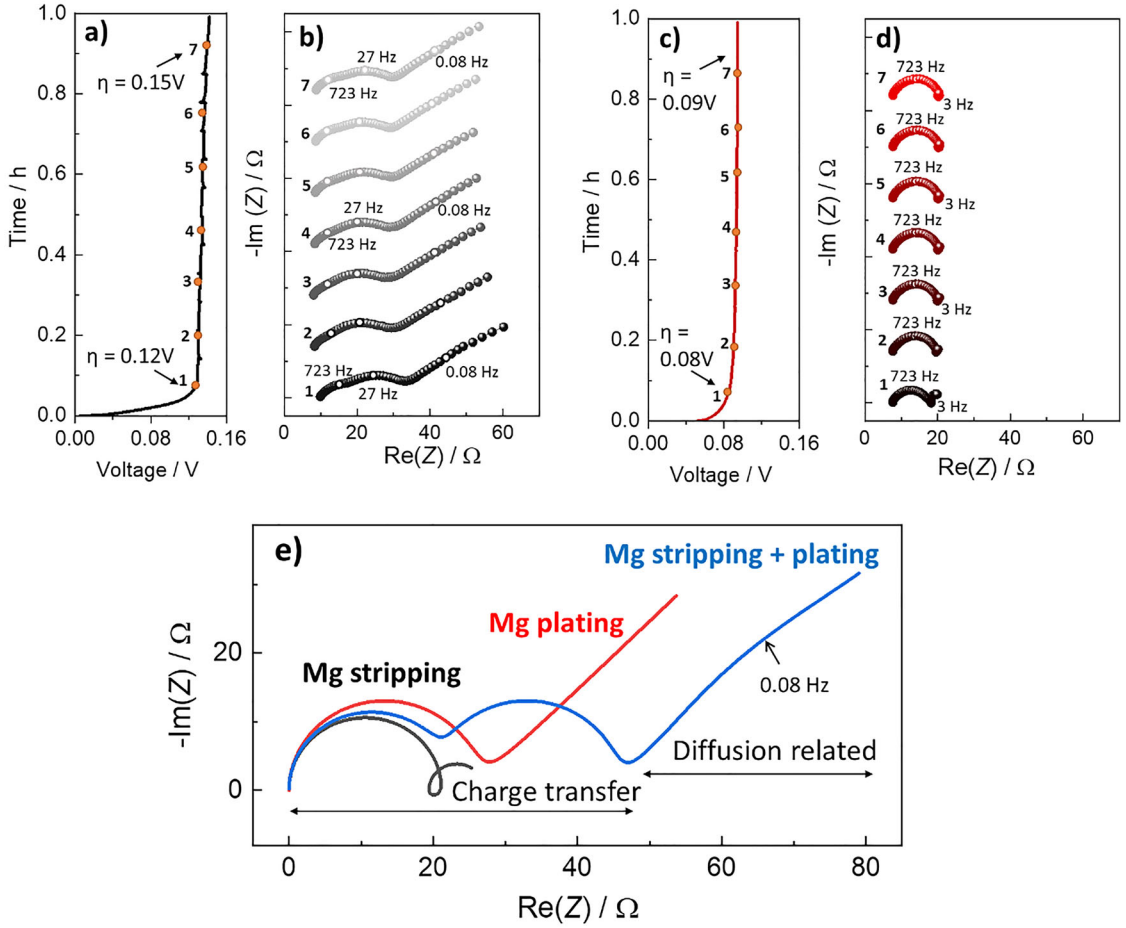

FIGURE 4 | (a) Voltage profile of the 10th cycle and (b) the corresponding *operando* EIS spectra for Mg||Mg 2E cells cycled in G2 electrolyte. (c) Voltage profile of the 10th cycle and (d) the corresponding *operando* EIS spectra for Mg||Mg cells cycled in G2-FDOL electrolyte. (e) Simulated EIS spectra for oxidized Mg electrode (stripping), reduced Mg electrode (plating), and for the complete cell (Mg stripping + plating) by using slightly changed model and conditions as in Figure 2 but with two changes assumed on the plated electrode: the morphology of the plated electrode is assumed to be porous with 27 times larger surface area than the geometrical value (calculated from the change in C_{dl} values). The pores lead to transport complications (diffusion of active species), which give rise to the finite length diffusion resulting in the 45° line at the lowest frequencies. More modeling details are provided in Note S9.

of various morphologies, which introduce significant differences to the active surface area of the electrode, as well as pose as an additional transport limitation. At this point, significant differences in overpotentials were observed (see Figure 1c), with the corresponding EIS results displayed in Figure 4. The G2 electrolyte exhibits a high overpotential of approximately 0.15 V (Figure 4a), accompanied by a substantial change in impedance characteristics, including the emergence of a sloped line at low frequencies (Figure 4b). In contrast, the G2-FDOL electrolyte maintains a stable overpotential of 0.09 V (Figure 4c) and a low total resistance of approximately 22 Ω, with no additional features if compared to the first half cycle analysis (Figure 4d). A similar low-frequency feature as evident in the G2 electrolyte in the 10th cycle, appears in the G2-FDOL electrolyte after extended cycling (60th cycle, Figure S32).

The frequency range where the new feature is observed is correlated with diffusional transport. Its appearance is also closely correlated to the appearance of short circuits, which happen shortly after the detection of these diffusion-related contributions. A similar diffusional tail has also been observed in the impedance response of Mg metal cycled in other Mg electrolytes at OCV after cycling, as reported in recent publications [30, 31, 58]. However, these works did not explicitly study its contribution to the EIS spectra. As explained in Note S11 and Figures S23–S38, the Mg anode that underwent plating is responsible for the diffusion-related impedance observed in the *operando* EIS spectra during extended cycling in Mg||Mg cells. This resembles the case of Mg electrodes in aqueous solutions [59], where, in addition to the kinetics (which is similar to the present model except that there is only one adsorbed intermediate), diffusion into cracks in the passive film also determines the electrode dynamics. Indeed, after prolonged cycling, diffusional complications can also occur in the pores of the deposits in the present case, as demonstrated before. This case is simulated by using the model presented before, and the results are shown in Figure 4e, in which the so-called Warburg impedance, which describes the diffusion of active species in the pores of the deposited film, is added (for details, see Note S9). It was also assumed that the surface area of the porous film is about 30 times larger than the geometric surface area (based on the difference in time constants in the measurements). These two relatively moderate changes

16146840, 2026, 18, Downloaded from https://advanced.onlinelibrary.wiley.com/doi/10.1002/aenm.202506415 by Ervin Rems - Bibliothèque de Sorbonne Université , Wiley Online Library on [15/05/2026]. See the Terms and Conditions (https://onlinelibrary.wiley.com/terms-and-conditions) on Wiley Online Library for rules of use; OA articles are governed by the applicable Creative Commons License

already lead to a fairly good agreement between the simulated spectrum and the actual measurements in G2 electrolyte after 10 cycles (see Figure 4b). Our findings, therefore, show that the Mg anode undergoing plating is primarily responsible for the increase in overpotential. Thus, we hypothesize that prolonged cycling leads to the formation of passivated Mg deposits, resulting in an increase of diffusion-related impedance.

This hypothesis was investigated using scanning electron microscopy (SEM) and high-resolution X-ray photoelectron spectroscopy (XPS) to analyze the Mg deposits on the plated Mg surface in different electrolytes. Figure S39a presents photographs of the Mg stripped and plated electrodes extracted from Mg||Mg cells after the 10th cycle of Mg plating/stripping, showing a nearly identical surface coverage of Mg deposits. In this case, Mg deposits were also observed on the plated Mg anode (i.e., not all remained on the separator). While both electrolytes produced similar morphologies and surface coverage of Mg deposits on the plated Mg anode (Figure S39b,c), they differed significantly in the thickness of the deposits. For instance, the G2 electrolyte resulted in thicker deposits (~11 µm, Figure S39d) compared to the G2-FDOL electrolyte (~2 µm, Figure S39e). However, this does not represent the full thickness of Mg deposits, as some deposits adhered to the separator, as seen in Figure S39a. These adhered deposits had a thickness of ~4 and 7 µm for G2 and G2-FDOL electrolytes, respectively (Figure S40). Summing both contributions, the total Mg deposit thickness is approximated to 16 µm in the G2 electrolyte and to 9 µm in the G2-FDOL electrolyte. It should be noted that plating 2 mAh cm^{-2} of Mg corresponds to a theoretical dense thickness of approximately 5.22 µm. The larger thicknesses measured experimentally are therefore reasonable, as the Mg deposits are porous rather than dense and may grow into the separator pores.

To validate these observations, focused ion beam SEM (FIB-SEM) coupled with EDS was used to examine cross-sections of Mg anodes cycled for 10 cycles in both electrolytes (Figure 5a,b). The Mg anode cycled in the G2 electrolyte exhibited thick Mg deposits that extended through the separator (Figure 5a), consistent with the ex situ SEM results. In contrast, the Mg anode cycled in the G2-FDOL electrolyte showed virtually no Mg deposits penetrating the bulk of the separator (Figure 5b). We therefore attribute the diffusion-related features observed at low frequencies in the operando EIS spectra of Mg anodes cycled for 10 cycles in G2 to the thick Mg deposits blocking the separator pores. The reduced thickness of Mg deposits, coupled with the improved Mg plating/stripping in the G2-FDOL electrolyte, explains its lower overpotentials and impedance at the 10th cycle, as observed in Figure 4.

Additionally, a magnified view of the Mg surface cycled in the G2 electrolyte revealed the formation of a porous MgO passive film (Figure S41), which is approx. 2 µm thick. We cannot rule out that this layer also contributes to the diffusional limitations of the cell. Although it is thinner, its structure is more closed, which suggests that the transport through this layer can have EIS features in the same frequency range. To further characterize the surface of the electrodes, XPS spectra of the Mg metal surface were measured after the 1st and 10th cycles, revealing that similar chemical species are present on the Mg surface in both electrolytes, though in different quantities (Figure 5c–g; Figure S42, see also Note S12 for detailed attributions of different species). We summarized the atomic percentages, binding energies, and chemical attribution of each species observed in the XPS spectra for each element in Table S3. In the first half cycle (Figure S42a), the Mg *2p* spectra reveal a significantly higher amount of metallic Mg (Mg^0) on the Mg anode cycled in G2-FDOL compared to in the G2 electrolyte. The C *1s* and F *1s* spectra XPS spectra (Figure S42b,d) indicate a similar type and amount of carbon- and fluorine-containing species, while for oxygen species, a difference in MgO content is detected with larger signals in the G2 electrolyte (Figure S42c). Overall, during the first half cycle of Mg plating/stripping, only minimal differences between the surface composition of Mg deposits were observed. These results align well with the observation that both electrolytes exhibit similar CIPs (Figure 1e) and therefore produce comparable amounts of inorganic decomposition products during initial cycling. However, the higher Mg° content in G2-FDOL electrolyte suggests a thinner passive layer in G2-FDOL electrolyte. To further support this, the thickness of the Mg passive film was calculated from the EIS data shown in Figure S25. The calculated Mg passive layer thicknesses for the G2 and G2-FDOL electrolytes were approximately 1.5 and 0.9 nm (the calculations are shown in Note S13), respectively, which are consistent with literature reports for Mg passive films formed at OCV [31, 60]. These results indicate that the G2-FDOL electrolyte forms a thinner passive layer on the Mg metal anode. This likely contributes to the more uniform electrode activation observed by *operando* EIS and SEM during the first half cycle.

After 10 cycles of Mg plating and stripping, we observed larger differences in the composition of chemical species on the Mg metal surface. For instance, the Mg^0 peak (Figure 5c) almost completely disappeared in the Mg *2p* XPS spectra of Mg metal cycled in G2 electrolyte, whereas the signals from Mg^0 were still observed in G2-FDOL. The C *1s* spectra (Figure 5d) showed similar ratios of solvent decomposition products (C—O, COO and CF_3) in both electrolytes. Additionally, the O *1s* spectra (Figure 5e) revealed higher MgO content, while the F *1s* spectra (Figure 5f) showed an increased amount of MgF_2 in G2 electrolyte. These findings suggest that the Mg deposits in G2 are more inorganic in nature compared to those in G2-FDOL, where it appears to facilitate more stable Mg plating with fewer anion decomposition products. Considering that MgF_2 and MgO are the primary inorganic species [61] and C—C/C—H, C—O, and COO groups are the main organic species originating from solvent decomposition [30, 62], it can be concluded that the G2 electrolyte undergoes substantial decomposition, as evidenced by the high concentration of both inorganic and organic species (Table S3) [63]. In contrast, the G2-FDOL electrolyte exhibits relatively stable composition, maintaining a consistent distribution of species even after the 10th Mg plating/stripping cycle (Table S3). We attribute the differences to the FDOL addition suppressing salt decomposition (evident in G2 electrolyte) through increasing Mg^{2+}-G2 interactions. This supports the EIS analysis, where the reason for the overpotential increase was indicated to be the diffusional constraints due to transport of ions in the electrolyte inside the passivated porous high surface area Mg deposits. Note that MgF_2 present in the passivation layer is attributed to anion decomposition and not to the FDOL interaction. The term "fluorinated" in the context of the title of this study, therefore, refers to the FDOL molecular identity and physicochemical properties, but does not imply that it produces fluorine rich interfacial layers.

16146840, 2026, 18, Downloaded from https://advanced.onlinelibrary.wiley.com/doi/10.1002/aenm.202506415 by Ervin Rems - Bibliothèque de Sorbonne Université , Wiley Online Library on [15/05/2026]. See the Terms and Conditions (https://onlinelibrary.wiley.com/terms-and-conditions) on Wiley Online Library for rules of use; OA articles are governed by the applicable Creative Commons License

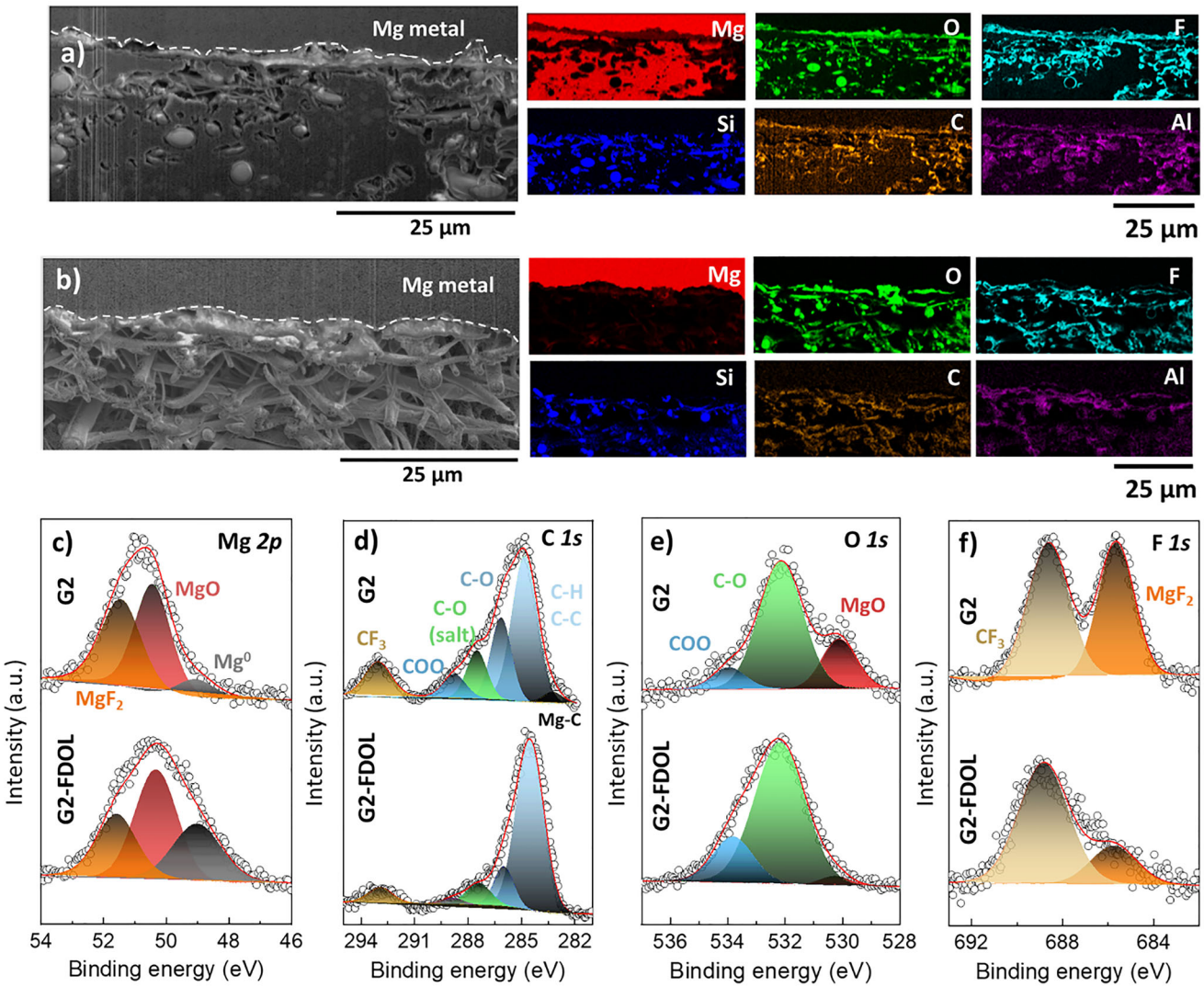

FIGURE 5 | FIB-SEM cross-sectional images and their corresponding EDS maps of the plated Mg anode cycled for 10 cycles in (a) G2 and (b) G2-FDOL. XPS spectra measured on Mg anode cycled for 10 cycles in different electrolytes for (c) Mg *2p*, (d) C *1s*, (e) O *1s*, and (f) F *1s*. All the Mg anodes were extracted from Mg||Mg cells cycled for the 10^{th} cycle at a current density of 2 mA cm^{-2} to a cutoff capacity of 2 mAh cm^{-2}.

In summary, during the first Mg plating, both electrolytes exhibit similar chemical compositions (XPS) but differ in morphology (SEM). The passivation layer in G2-FDOL electrolyte is thinner, which leads to improved and more uniform electrode activation (breakage in the passive layer). This explains its lower initial charge transfer resistance and overpotentials. Chemically, the FDOL electrolyte promotes the formation of a passive film with less inorganic content (MgO and MgF_2, which originate from the decomposition of Alhfip$^-$). FDOL indirectly causes this through the changes in the electrolyte solvation structure. Mg deposition in G2 is less smooth with high surface area deposits, which reduces the initially high overpotentials and shows as EIS spectra change in the high frequency region.

With prolonged cycling, the electrolyte differences become more pronounced. The G2 electrolyte leads to the formation of thicker Mg deposits (as confirmed by SEM) that are primarily inorganic in nature, consisting of higher amounts of MgO and MgF_2 (as indicated by XPS). These passivated deposits hinder transport of active ions to the electrode and significantly increase impedance (as indicated by EIS and an increase in low-frequency contributions). In contrast, the G2-FDOL electrolyte produces thinner passivation layers and more uniform Mg deposits, which remain electrochemically active (higher proportion of Mg^0 detected by XPS, no transport issues seen in EIS). If the deposits are active, diffusional resistances are small, since species need to travel only for a short distance before reaching the active electrode surface (i.e., these are distances on the order of pore size, nm-sized). If the deposits are fully passivated (sometimes referred to as "dead" [57, 64]), then these deposits act as an additional separator, where the species need to travel through the whole thickness (µm-sized) before reaching the active electrode surface, providing significant diffusional limitations. Note that the situation on the electrode is changing during operation (stripping from active deposits produces "dead" deposits), while at the same time, the active deposits are getting continuously passivated through the side reactions with the electrolyte. In practice, the more electrochemically active Mg deposits for G2-FDOL electrolyte enable sustained, efficient transport and electrochemical reactions at the Mg metal surface, thereby maintaining lower impedance (as shown in Figures 3

16146840, 2026, 18, Downloaded from https://advanced.onlinelibrary.wiley.com/doi/10.1002/aenm.202506415 by Ervin Rems - Bibliothèque de Sorbonne Université , Wiley Online Library on [15/05/2026]. See the Terms and Conditions (https://onlinelibrary.wiley.com/terms-and-conditions) on Wiley Online Library for rules of use; OA articles are governed by the applicable Creative Commons License

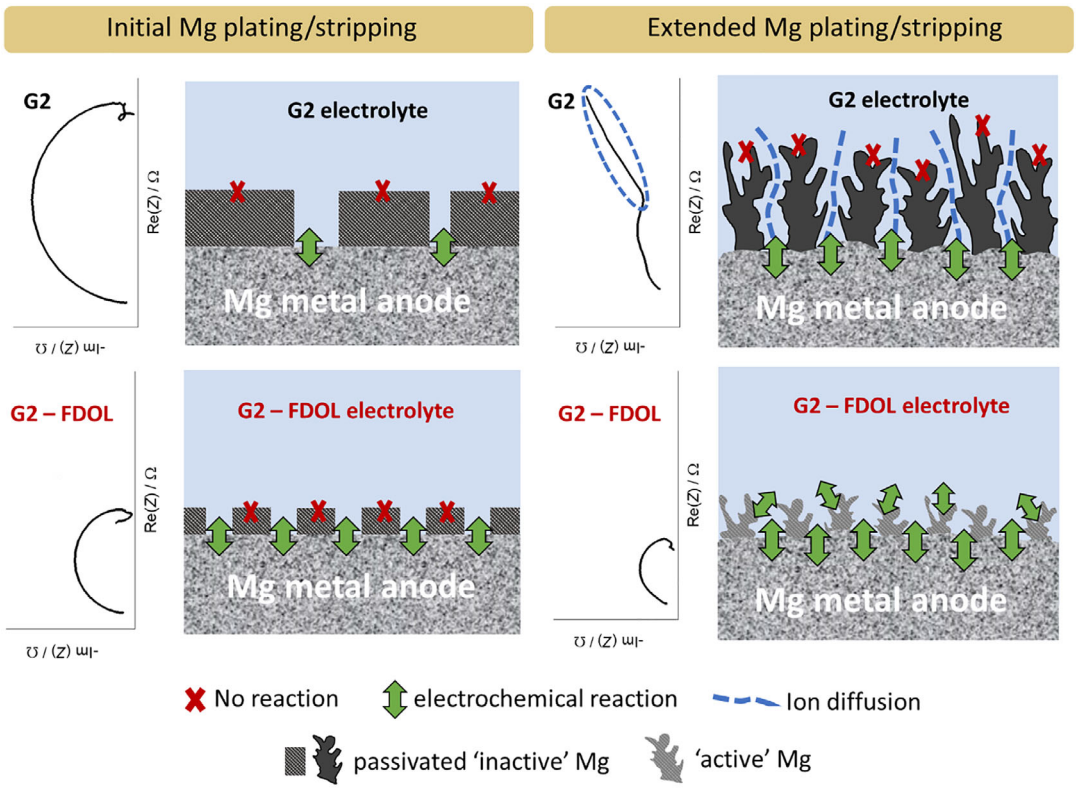

FIGURE 6 | Schematic representation of the electrochemical processes governing impedance at the cycled Mg anode during initial and extended cycles of Mg plating/stripping in different electrolytes. Please note that the scheme presented here is neither exhaustive nor to scale.

and 4). The overall mechanism is schematically illustrated in Figure 6.

3 | Conclusions

In this study, we investigated the use of cyclic fluorinated ether FDOL in $Mg[Al(hfip)_4]_2$/G2 electrolyte. We found that 10 vol.% of FDOL addition significantly improves the overall electrochemical performance of Mg metal in high-voltage RMBs (PANI cathode). Since EIS at OCV gives limited information on the electrochemical processes occurring on Mg metallic anodes, we employed *operando* EIS to investigate the mechanisms underlying the observed performance enhancement in G2-FDOL electrolytes. *Operando* EIS of the G2-FDOL electrolyte revealed a similar interfacial mechanism to that of the G2 electrolyte; however, the enhanced performance is attributed to a more uniform activation of the electrode surface and improved Mg plating morphology. This was supported by FIB-SEM and XPS analysis, where decreased decomposition of G2-FDOL electrolyte on Mg metal was found. The origin of the difference is attributed to a change in magnesium solvation environment, which originates from the diluent nature of FDOL, increasing the interaction of Mg^{2+} with G2 and decreasing anion decomposition. FDOL, therefore, effectively decreases MgF_2 content in Mg passive film. This facilitates sustained ionic transport and more efficient interfacial electrochemical reactions, thereby contributing to the lower impedance observed in *operando* EIS measurements. Our results highlighted: (i) the potential of using fluorinated ethers in Mg electrolytes for stabilizing Mg metallic anodes as well as high-voltage cathodes in RMBs, thus contributing toward the electrolytes development for high-voltage RMBs, and (ii) the power of *operando* EIS in providing more information on the electrochemical processes occurring on the Mg metal/electrolyte interfaces.

4 | Experimental

4.1 | Synthesis of Salt and Electrolytes

Salt synthesis and electrolyte preparation were conducted under an inert atmosphere within an Ar-filled glovebox, maintaining O_2 and H_2O levels below 1 ppm. The $Mg[Al(hfip)_4]_2$ salt was synthesized following a previously reported procedure [26], with modifications in the final salt isolation step. Specifically, 1,1,1,3,3,3-hexafluoroisopropanol (hfipH) (2.5 equivalents relative to Mg; Apollo Scientific, 99.9%) was added dropwise to a 1.0 M n-Bu_2Mg/heptane solution (Sigma–Aldrich). The solvent and residual hfipH were then removed under vacuum, yielding a white crystalline powder, $Mg(hfip)_2$. This compound was subsequently dissolved in 1,2-dimethoxyethane (monoglyme, G1; Sigma–Aldrich, ReagentPlus, ≥99%, inhibitor-free), followed by the addition of a 2.0 M $Al(CH_3)_3$/toluene solution (2.02 equivalents relative to Mg; Sigma–Aldrich), and excess hfipH (3.5 equivalents relative to Al) was introduced for 1 h. The reaction proceeded under continuous stirring at room temperature for 24 h. Upon completion, solvents and residual reactants were removed under vacuum to obtain a concentrated solution, which

16146840, 2026, 18, Downloaded from https://advanced.onlinelibrary.wiley.com/doi/10.1002/aenm.202506415 by Ervin Rems - Bibliothèque de Sorbonne Université , Wiley Online Library on [15/05/2026]. See the Terms and Conditions (https://onlinelibrary.wiley.com/terms-and-conditions) on Wiley Online Library for rules of use; OA articles are governed by the applicable Creative Commons License

was then slowly introduced into hexane to induce precipitation of the $[Mg(G1)_3][Al(hfip)_4]_2$, later denoted as $Mg[Al(hfip)_4]_2$ salt. The precipitated salt was collected via filtration and subjected to vacuum drying at 45°C for 24 h.

The $Mg[B(hfip)_4]_2$ salt was synthesized following a previously reported procedure [25], with a modification in the salt isolation step. The hfipH (2.05 equiv relative to Mg; 1.1 mL, 10.3 mmol) was added dropwise to a 1.0 M solution of n-Bu_2Mg in heptane (5.0 mL, 5.0 mmol) over a period of 30 min. The solvent and residual hfipH were removed under vacuum, yielding a white crystalline powder, $Mg(hfip)_2$. The resulting solid, $Mg(hfip)_2$, was dissolved in 10 mL of G1, and the solution was stirred for 30 min. Subsequently, 1.0 M BH_3-THF (Sigma Aldrich, 2.2 equiv relative to Mg; 11 mL, 11 mmol) was added dropwise to the $Mg(hfip)_2$/G1 solution over 30 min, followed by the dropwise addition of hfipH (3.1 equiv relative to B; 3.6 mL, 34.1 mmol) over 1 h. The reaction mixture was then stirred vigorously for 24 h. After completion, the solvent and excess hfip-H were removed under reduced pressure to obtain a concentrated solution, which was slowly added to hexane to induce precipitation of the $[Mg(G1)_3][B(hfip)_4]_2$ salt, later denoted as $Mg[B(hfip)_4]_2$ salt. The precipitate was filtered and dried under vacuum at 45°C for 48 h.

Electrolyte preparation involved drying and purification of solvents to minimize water content. G2 (Acros Organics, 99%, extra pure) and DOL (Sigma–Aldrich, HPLC grade, 99.9%) solvents were dried using 4 Å molecular sieves for five days, refluxed overnight with a Na/K alloy, and subsequently purified by fractional distillation. Similarly, the fluorinated ethers such as BTFE (Sigma Aldrich), TTE, TFDOL, and FDOL (all are from Apollo Scientific, 99%) were dried over 4 Å molecular sieves for ten days. The water content in all solvents was determined by Karl Fischer titration (Mettler Toledo, C20) and confirmed to be below 0.1 ppm. Electrolytes were prepared by accurately weighing stoichiometric amounts of $Mg[Al(hfip)_4]_2$, $Mg(TFSI)_2$, $MgCl_2$, $Mg(OTf)_2$ salts into a volumetric flask, dissolving them in a small volume of G2 solvent or a G2-BTFE, G2-TTE, and G2-BTFE solvent mixtures, and then diluting to the marked volume. In some cases, the electrolyte composition was systematically varied by adjusting the G2-FDOL volume ratios while maintaining a constant salt concentration of 0.4 M.

4.2 | Preparation of Electrodes and Cell Assembly

Mo_6S_8 was synthesized by high-temperature annealing of elemental copper, molybdenum, and sulfur. A 5 g mixture with excess sulfur, corresponding to the stoichiometry $Cu_2Mo_6S_{8.5}$, was prepared and loaded into Swagelok stainless-steel vessels inside an argon-filled glovebox. The sealed vessels were then placed in a preheated furnace and annealed at 1000°C for 20 min, using a reactant-to-reactor volume ratio of 1:2. After cooling, the resulting product was ground into a fine powder with submicrometer-sized particles using a mortar and pestle and characterized by X-ray diffraction, confirming the formation of the copper Chevrel phase. Copper was subsequently removed via a mild chemical oxidation using an I_2/acetonitrile solution, yielding the Mo_6S_8 cathode material.

A carbon/sulfur (C/S) composite was prepared by planetary ball milling (Retsch PM100) using Ensaco 350 G carbon (Imerys) and sulfur in a mass ratio of 66:33. The mixture was milled at 300 rpm for 30 min and subsequently subjected to a melt-diffusion impregnation step. The milled powder was heated to 155°C under an argon atmosphere at a controlled heating rate of 0.2°C min^{-1} and held at this temperature for 5 h to facilitate sulfur infiltration into the carbon matrix. The composite was then cooled to room temperature at a rate of 0.5°C min^{-1}. PHBQS was synthesized based on the procedure already described in the literature [65]. PANI (emeraldine base, average $M_w \sim 50\,000$) was purchased from Sigma Aldrich and used as an organic active material for the cathode preparation.

All cathodes were prepared by blending active material (Mo_6S_8, PHBQS, and PANI), carbon black (Printex XE2, Degussa), and polytetrafluoroethylene (PTFE) binder (Sigma Aldrich, 60% water dispersion) in a mass ratio of 60:30:10. However, sulfur cathodes were prepared by mixing C/S composite, C65 carbon black, and PTFE binder in the same mass ratio. The components were dispersed in isopropanol and subjected to ball milling (30 min, 300 rpm, Retsch PM100). The prepared black gum-like composite was further mixed using a mortar to ensure uniformity. The electrode composite was subsequently processed by rolling between a glass plate and parchment paper to produce self-standing electrodes with an active material loading in the range of: 2.0–3.2 mg cm^{-2} for Mo_6S_8, ~1 mg cm^{-2} for S, and 2.5 – 3.0 mg cm^{-2} for both PHBQS and PANI organic cathodes. All the cathodes were punched into discs with 12 mm diameters and dried at 50°C overnight before they were transferred to the glove box.

All cell preparation was conducted inside an argon-filled MBraun glovebox in a 2E Swagelok-type cell. In all configurations, Mg metal anodes (polished with P1200 sandpaper) with a diameter of 12 mm were employed. Two glass fiber separators (Whatman GF/A, 13 mm in diameter) soaked with 75 µL of electrolyte were used as the primary separators. In some cases, an additional pair of Celgard 2320 separators (13 mm in diameter), soaked with 15 µL of electrolyte, was placed adjacent to the Mg anodes. Three-electrode (3E) Mg||Au||Mg and Mg||Au||PANI cells were assembled in T-type Swagelok configurations, using a gold wire (Goodfellow, 50 µm thickness, 0.7 µm polyimide insulation) as a pseudo-reference electrode. The Mg and PANI electrodes used in 3E cells were 10 mm in diameter. Stainless steel discs were employed as current collectors on both sides of the electrodes in all experiments.

4.3 | Electrochemical and Materials Characterization

The CE of Mg plating/stripping was evaluated in Mg||Pt cells using macroreversibility measurements [48, 66]. For this purpose, a Mg reservoir was first plated onto the Pt electrode with a capacity of 5 mAh cm^{-2} (Q_T). Subsequently, 1 mAh cm^{-2} (Q_C) of Mg was cycled through repetitive stripping and plating for n cycles (30 cycles), followed by complete stripping of the entire Mg from the Pt electrode until a cutoff voltage of 2 V was reached. The final stripping charge (Q_S) was measured. Throughout the

16146840, 2026, 18, Downloaded from https://advanced.onlinelibrary.wiley.com/doi/10.1002/aenm.202506415 by Ervin Rems - Bibliotheque de Sorbonne Universite , Wiley Online Library on [15/05/2026]. See the Terms and Conditions (https://onlinelibrary.wiley.com/terms-and-conditions) on Wiley Online Library for rules of use; OA articles are governed by the applicable Creative Commons License

entire procedure, the current density was fixed at 1.0 mA cm^{-2}. The average CE was determined using the following equation:

$$CE = \frac{nQ_C + Q_S}{nQ_C + Q_T} \quad (5)$$

The cycling stability of Mg plating/stripping CE was assessed in Mg||Pt cells at a current density of 1.0 mA cm^{-2} with a cutoff areal capacity of 1.0 mAh cm^{-2}. To investigate the oxidative stability of the electrolytes, LSV was performed using Mg||Pt and Mg||carbon-coated Al cells at scan rates of 0.1 and 0.5 mV s^{-1}. Additionally, the cycling stability of Mg plating and stripping was evaluated in Mg||Mg symmetric cells at different current densities of 0.1, 1.0, and 2.0 mA cm^{-2}, with corresponding cutoff areal capacities of 0.1, 1.0, and 2.0 mAh cm^{-2}, respectively. EIS was carried out at OCV in the frequency range of 1 MHz – 20 mHz with an rms amplitude of 10 mV. *Operando* EIS was carried out on Mg||Mg 2E and 3E cells at a current density of 2.0 mA cm^{-2} with a cutoff areal capacity of 2.0 mAh cm^{-2}. We selected this testing condition because we observed significant differences in the electrochemical performance of different electrolytes at earlier stages of Mg plating/stripping cycles. For this purpose, galvanostatic EIS measurements were conducted using a current amplitude of 0.2 mA (I_{DC}/10) over a frequency range of 1 MHz to 20 mHz. A total of 14 impedance spectra were recorded during each half-cycle, with each spectrum acquisition lasting approximately 4.5 min. For the sake of better visibility, we displayed seven impedance spectra in the *operando* EIS graphs in the continuation. Mg||PANI cells were tested in a voltage range of 0.5 – 3.5 V vs. Mg^0/Mg^{2+} at charge/discharge rates of 0.1, 0.5, 1.0, and 2.0 C, whereas a 1.0 C-rate was used for Mg||Au||PANI 3E cells. Mg||Mo_6S_8, Mg||S, and Mg||PHBQS cells were tested within voltage ranges of 0.5 – 2.0 V, 0.1 – 2.5 V, and 1.0 – 3.0 V vs. Mg^0/Mg^{2+}, respectively, at current rates/densities of 0.1 or 1 C (Mg||Mo_6S_8), 0.1 C (Mg||S), and 50 mA g^{-1} (Mg||PHBQS). All the electrochemical tests were performed on VMP3 Bio-logic potentiostats/galvanostats.

Raman measurements of the solvents and electrolytes were performed using a Bruker Ram II spectrometer with a 1064 nm excitation laser. Each spectrum represents an average of 512 scans recorded at a resolution of 4 cm^{-1} over the 50 – 3600 cm^{-1} range. Samples were sealed in airtight quartz tubes (1 cm path length) under an argon atmosphere to prevent exposure to air or moisture during measurement. IR characterization was performed inside an argon-filled glovebox using an ATR-IR Alpha II (Bruker) spectrometer equipped with a diamond crystal. Spectra were collected at room temperature by averaging 48 scans over the range of 4000–400 cm^{-1} with a spectral resolution of 4 cm^{-1}.

The ex situ analysis of the cycled Mg||PANI and Mg||Mg cells was carried out using SEM coupled with EDS and XPS. For this analysis, cycled Mg anodes (either after the first half cycle or the tenth cycle) were extracted from the cells and carefully washed with a few drops of anhydrous G2 solvent for approximately 20 s to remove residual electrolyte salt while minimizing unintended surface damage due to handling. The morphology of the PANI cathode and Mg deposits was examined using SEM (SUPRA 35VP, Zeiss, Germany). To prevent atmospheric exposure, the samples were transferred to the SEM chamber using a vacuum transfer tool. The acceleration voltage was set to 1.5 kV for SEM imaging and 10 kV for EDS. PANI electrodes were analyzed using similar conditions: accelerating voltage 10 keV, beam current 40 nA, Oxford Instruments Ultim Max 100 detector.

For UV–vis measurements, PANI electrodes were charged to 3.5 V or discharged to 0.5 V, to evaluate solubility in different redox states. For comparison, Li||PANI cell with LP40 (1 M $LiPF_6$ in EC/DEC (1/1 vol.%)) was also assembled using the same cell parameters ad Mg||PANI (PANI loading, separator type, electrolyte amount, etc.). After cycling at C/2, the electrodes were harvested from the cells, weighed, and 7 mg of the composite was added to a flask, with 300 µL of the electrolyte in which the electrode had been cycled. Electrodes were left to soak for 24 h and then filtered and diluted with G2, G2-FDOL or EC/DEC to a final volume of 3 mL. The samples were closed in quartz cuvettes inside the glovebox and transferred to the instrument. Measurements were performed on a PerkinElmer LAMBDA 950 spectrometer in the range of 400–850 nm.

FIB cross-sectional analysis was performed by using a FIB-SEM Helios G5 UC equipped with a multi gas injection system (GIS), an CleanConnect sample transfer system (Thermo Fisher Scientific, The Netherland) and Ultim max 65 EDX detector (Oxford, UK). Samples were mounted into a CleanConnect capsule inside Ar filled glovebox and transferred in Ar atmosphere (200 mbar overpressure) directly to FIB instrument. The cross-section was performed with focused Ga+ ions at 30 kV @ 21 nA, with the FIB currents reduced stepwise to 0.4 nA for the final ion polishing step. Morphological images of the cross sections were recorded using a low-energy electron beam (1 kV @ 50 pA) by using standard ETD and ICE detectors. Detailed information at the SEI region was acquired using InColumn integrated TLD detector and a pre-monochromated electron beam at 500 V energy and 6.3 pA beam current. Low-energy EDX mapping (TruMap) was recorded at 5 kV energy and 0.8 nA beam current.

For XPS, the washed samples were transferred from the glovebox using Ar-filled transfer vessels. The XPS analysis was conducted using a VersaProbe III AD (Phi, Chanhassen, US) equipped with a monochromatic Al Kα_1 X-ray source (hν = 1.4867 eV). Spectra were collected from a 200 µm diameter analysis area, with the charge neutralizer activated to mitigate differential charging, as the electrodes were mounted on a non-conductive double-sided tape. High-resolution spectra were acquired with a pass energy of 69 eV and a step size of 0.05 eV. Charge neutralization was employed, and the energy scale of the XPS spectra was calibrated by referencing the C *1s* peak of carbon to a binding energy of 284.8 eV. During each measurement cycle, the Mg *2p*, C *1s*, O *1s*, and F *1s* core-level regions were recorded with a step size of 0.13 eV and a pass energy of 69 eV. Spectral analysis was performed using ULVAC-PHI Multipak software, with a binding energy uncertainty of ±0.3 eV for all peak fittings. Background correction was applied using either Shirley's or Smart's method. Instrumental broadening was assumed to be consistent across all regions; thus, the Gaussian fraction of each primary peak was fixed at 90%. The full width at half maximum (FWHM) for the main fitted peaks in the C *1s* region was constrained to 1.5 ± 20%. For all spectra fitting, we used the Gauss–Lorentz function [67] except Mg *2p* where we used an asymmetric function [67, 68] to fit it due to the metallic Mg (Mg^0) peak observed in its spectra.

16146840, 2026, 18, Downloaded from https://advanced.onlinelibrary.wiley.com/doi/10.1002/aenm.202506415 by Ervin Rems - Bibliothèque de Sorbonne Université , Wiley Online Library on [15/05/2026]. See the Terms and Conditions (https://onlinelibrary.wiley.com/terms-and-conditions) on Wiley Online Library for rules of use; OA articles are governed by the applicable Creative Commons License

4.4 | Simulation Methods

Frontier orbital energies (HOMO/LUMO) were obtained from gas-phase DFT calculations (vacuum reference, no implicit solvent) to compare the intrinsic oxidative stability of the solvents and quantify how orbital energies shift upon direct Mg^{2+} contact. The analysis included (i) Isolated solvents: fully optimized G2 and FDOL molecules in the gas phase and (ii) Ion-solvent contact pairs: fully optimized Mg^{2+}-G2 and Mg^{2+}-FDOL pairs in the gas phase to quantify frontier orbital perturbations arising from direct Mg^{2+} inner-sphere contact/coordination alone, not full solvation complexes or condensed-phase environments. All calculations were performed using Gaussian software [69] at the B3LYP/6-311+G(d,p) level of theory [70, 71]. Optimized structures exhibited no imaginary frequencies, confirming stationary points.

Classical MD simulations were conducted to explore the solvation environment of magnesium ions (Mg^{2+}) in relation to the anion $[Al(hfip)_4]^-$ and the solvent molecules FDOL and G2. The primary aim was to investigate how the addition of FDOL influences the coordination environment of Mg^{2+} with solvent molecules. Simulations were performed with the LAMMPS (Large-scale Atomic/Molecular Massively Parallel Simulator) software package [72], using the non-polarizable OPLS-AA (Optimized Potentials for Liquid Simulations All-Atom) force field [73]. Molecular topology files, Lennard–Jones parameters, and bonded parameters were generated with the *LigParGen* server [74–76] and the *fftool* package [77]. To account for electronic screening effects and improve the description of interionic interactions, a uniform charge scaling factor of 0.8 was applied to all ions, following established practice for non-polarizable force fields [78, 79]. Electrostatic interactions were treated with the particle-particle-particle-mesh (PPPM) method (accuracy 10^{-5}), with periodic boundary conditions applied in all three directions. The simulation protocol began with an energy minimization using the conjugate gradient method. This was followed by three equilibration stages: (i) NVT equilibration at 300 K for 2.5 ns with a time step of 0.5 fs, controlled by a Nosé-Hoover thermostat (relaxation time 100 fs); (ii) NPT equilibration (loose barostat) at 0.5 bar and 300 K for 2.5 ns, where an additional drag term was introduced to suppress large instantaneous pressure oscillations when the system density was still far from equilibrium; and (iii) NPT equilibration (target pressure) at 1 bar and 300 K for 5.0 ns. Following equilibration, production simulations were carried out in the NVT ensemble at 300 K, using a reduced time step of 0.25 fs. Each trajectory was propagated for 16 ns, with system properties recorded every 100 fs. RDFs were computed for cation-anion, cation-solvent, and group-specific atom pairs (500 bins, maximum distance 12 Å).

To move beyond static structural descriptors, we quantified both transport and solvation dynamics across the electrolytes. Self-diffusion coefficients were extracted from the diffusive regime of the mean-squared displacements using the Einstein relation:

$$D_i = \frac{1}{2} \lim_{t \to \infty} \frac{d}{dt} \left\langle \left(\mathrm{R_i}(t) - \mathrm{R_i}(0) \right)^2 \right\rangle \tag{6}$$

where $\mathbf{R_i}(t)$ is the position of the i-th at the time t, and the brackets denote the ensemble average. Reliable estimation requires sufficiently long trajectories to ensure convergence to the uncorrelated diffusion limit, as the method assumes that ion displacements become statistically independent at long times. In parallel, Mg^{2+} solvation-shell dynamics were quantified using an intermittent residence correlation function:

$$\mathrm{C}(t) = \frac{\langle h(0)\, h(t+\tau) \rangle}{\langle h \rangle} \tag{7}$$

where $h(t) = 1$ when a specific Mg—O pair lies within the first solvation sphere, defined from the first minimum of the Mg—O RDF, and 0 otherwise. Because spatial proximity does not necessarily imply a stabilizing interaction in crowded electrolytes, this definition captures persistence of geometric contact regardless of its physical origin (e.g., coordination vs packing-induced proximity). We also computed integral residence times as:

$$\tau_{int} = \int_0^\infty C(t)\, dt \tag{8}$$

and estimated uncertainties via block-averaged standard errors. These metrics provide a quantitative measure of coordination persistence that can be compared across electrolytes. Please note that our MD simulations remain bulk and do not explicitly include an electrode or applied potential. However, free-energy profiles, accurate diffusion coefficients, and ab initio MD would be valuable for explicit interfacial reactivity, but outside of the scope of this study, and will be addressed in future work.

Simulations of impedance spectra and current–voltage curves (see Figures 3g and 4e; Notes S5–S8), based on the proposed analytical solutions, were performed using Python 3.13. The source code is available upon request.

Acknowledgements

HAI, RD, and SDT acknowledge the funding from the DESTINY PhD programme (European Union's Horizon 2020 research and innovation program under the Marie Skłodowska-Curie Actions COFUND Grant Agreement #945357) and the additional financial support by the Slovenian Research Agency ARIS (core program funding P2-0423). SDT acknowledges financial support by the Slovene Research Agency ARIS with research project Z2-4465 funding. AM would like to acknowledge funding support of the Slovene Research Agency (ARIS) through Scientists4future Slovenia (MSCA-COFUND-SE/2023). HAI, JB, OL, and RD would like to acknowledge funding support of the Slovenian Research Agency (ARIS) through the ADREBO project (N2-0279).

Conflicts of Interest

The authors declare no conflicts of interest.

Data Availability Statement

The data that support the findings of this study are available from the corresponding author upon reasonable request.

References

1. Y. S. Meng, V. Srinivasan, and K. Xu, "Designing Better Electrolytes," *Science* 378 (2022): abq3750, https://doi.org/10.1126/science.abq3750.

2. Y. Tian, G. Zeng, A. Rutt, et al., "Promises and Challenges of Next-Generation "beyond Li-Ion" Batteries for Electric Vehicles and Grid Decarbonization," *Chemical Reviews* 121 (2021): 1623–1669, https://doi.org/10.1021/acs.chemrev.0c00767.

16146840, 2026, 18, Downloaded from https://advanced.onlinelibrary.wiley.com/doi/10.1002/aenm.202506415 by Ervin Rems - Bibliotheque de Sorbonne Universite , Wiley Online Library on [15/05/2026]. See the Terms and Conditions (https://onlinelibrary.wiley.com/terms-and-conditions) on Wiley Online Library for rules of use; OA articles are governed by the applicable Creative Commons License

3. H. Zhang, L. Qiao, and M. Armand, "Organic Electrolyte Design for Rechargeable Batteries: from Lithium to Magnesium," *Angewandte Chemie, International Edition* 61 (2022): 202214054, https://doi.org/10.1002/anie.202214054.

4. O. Gohar, H. A. Ishfaq, M. A. Iqbal, et al., "Recent Advancements in High-Performance and Durable Electrodes Materials for Magnesium-Ion Batteries," *Coordination Chemistry Reviews* 538 (2025): 216702.

5. P. Canepa, G. Sai Gautam, D. C. Hannah, et al., "Odyssey of Multivalent Cathode Materials: Open Questions and Future Challenges," *Chemical Reviews* 117 (2017): 4287–4341, https://doi.org/10.1021/acs.chemrev.6b00614.

6. R. Davidson, A. Verma, D. Santos, et al., "Formation of Magnesium Dendrites during Electrodeposition," *ACS Energy Letters* 4 (2019): 375–376, https://doi.org/10.1021/acsenergylett.8b02470.

7. B. Yan, C. Karuppiah, K. Z. Walle, M. M. Abdelaal, M. Kotobuki, and L. Lu, "Review on Dendrite Formation of Mg Metal Anode and Its Prevention," *Nano Energy* 131 (2024): 110292, https://doi.org/10.1016/j.nanoen.2024.110292.

8. M. S. Ding, T. Diemant, R. J. Behm, S. Passerini, and G. A. Giffin, "Dendrite Growth in Mg Metal Cells Containing $Mg(TFSI)_2$ /Glyme Electrolytes," *Journal of the Electrochemical Society* 165 (2018): A1983–A1990, https://doi.org/10.1149/2.1471809jes.

9. R. Mohtadi, O. Tutusaus, T. S. Arthur, Z. Zhao-Karger, and M. Fichtner, "The Metamorphosis of Rechargeable Magnesium Batteries," *Joule* 5 (2021): 581–617, https://doi.org/10.1016/j.joule.2020.12.021.

10. J. Muldoon, C. B. Bucur, and T. Gregory, "Quest for Nonaqueous Multivalent Secondary Batteries: Magnesium and beyond," *Chemical Reviews* 114 (2014): 11683–11720, https://doi.org/10.1021/cr500049y.

11. R. Attias, M. Salama, B. Hirsch, Y. Goffer, and D. Aurbach, "Anode-Electrolyte Interfaces in Secondary Magnesium Batteries," *Joule* 3 (2019): 27–52, https://doi.org/10.1016/j.joule.2018.10.028.

12. L. Tong, J. Wang, J. Wang, B. Qu, G. Huang, and F. Pan, "Research Progress on Compatibility between Anode and Electrolyte of Rechargeable Magnesium Batteries," *Cailiao Daobao/Materials Reports* 37 (2023): 22040273–22040277, 10.11896/cldb.22040273.

13. J. D. Forero-Saboya, D. S. Tchitchekova, P. Johansson, M. R. Palacín, and A. Ponrouch, "Interfaces and Interphases in Ca and Mg Batteries," *Advanced Materials Interfaces* 9 (2022), https://doi.org/10.1002/admi.202101578.

14. O. Tutusaus, R. Mohtadi, N. Singh, T. S. Arthur, and F. Mizuno, "Study of Electrochemical Phenomena Observed at the Mg Metal/Electrolyte Interface," *ACS Energy Letters* 2 (2017): 224–229.

15. Q. Yang, J. Xu, L. Chen, Y. Gong, X. Sun, and C. Chen, "The Effects of $NaHCO_3$ on the Voltage Delay of Mg Cell with AZ31B Magnesium Alloy in $Mg(ClO_4)_2$ Electrolytic Solution," *Journal of the Electrochemical Society* 164 (2017): A630, https://doi.org/10.1149/2.0391704jes.

16. G. Hasegawa, Y. Akiyama, M. Tanaka, et al., "Reversible Electrochemical Insertion/Extraction of Magnesium Ion into/from Robust NASICON-Type Crystal Lattice in a $Mg(BF_4)_2$ -Based Electrolyte," *ACS Applied Energy Materials* 3 (2020): 6824–6833, https://doi.org/10.1021/acsaem.0c00943.

17. S. B. Son, T. Gao, S. P. Harvey, et al., "An Artificial Interphase Enables Reversible Magnesium Chemistry in Carbonate Electrolytes," *Nature Chemistry* 10 (2018): 532–539, https://doi.org/10.1038/s41557-018-0019-6.

18. Z. Lu, A. Schechter, M. Moshkovich, and D. Aurbach, "On the Electrochemical Behavior of Magnesium Electrodes in Polar Aprotic Electrolyte Solutions," *Journal of Electroanalytical Chemistry* 466 (1999): 203–217, https://doi.org/10.1016/S0022-0728(99)00146-1.

19. J. Muldoon, C. B. Bucur, A. G. Oliver, J. Zajicek, G. D. Allred, and W. C. Boggess, "Corrosion of Magnesium Electrolytes: Chlorides – the Culprit," *Energy & Environmental Science* 6 (2013): 482–487, https://doi.org/10.1039/c2ee23686a.

20. Y. Hao, D. Wang, Y. Chen, et al., "An Ultra-Thin Composite Magnesium Anode with Controlled (002) Facet Orientation by Heterogeneous Epitaxial Electrodeposition for Highly Stable Lean-Magnesium Metal Batteries," *Acta Materialia* 293 (2025): 121107, https://doi.org/10.1016/j.actamat.2025.121107.

21. Y. Chen, Z. Tang, B. Qu, et al., "A Universal Fluorinated Composite Interphase with Self-Healing Function Enabling Long-Cycling Rechargeable Magnesium Batteries," *Advanced Functional Materials* 35 (2025): 19580, https://doi.org/10.1002/adfm.202519580.

22. Y. Chen, X. Shen, J. Wang, et al., "Insights into Hyper-Efficient Construction of Compact Artificial SEI for Highly Reversible Mg Metal Anode," *ACS Energy Letters* 9 (2024): 5616–5626, https://doi.org/10.1021/acsenergylett.4c02123.

23. H. Dong, O. Tutusaus, Y. Liang, et al., "High-Power Mg Batteries Enabled by Heterogeneous Enolization Redox Chemistry and Weakly Coordinating Electrolytes," *Nature Energy* 5 (2020): 1043–1050, https://doi.org/10.1038/s41560-020-00734-0.

24. T. Pavčnik, M. Radi, O. Lužanin, et al., "Effect of Ligand Variation on Mg Alkoxyborate Electrolytes: Does More Fluorine Help?," *Journal of Power Sources* 626 (2025): 235711.

25. T. Mandai, "Critical Issues of Fluorinated Alkoxyborate-Based Electrolytes in Magnesium Battery Applications," *ACS Applied Materials & Interfaces* 12 (2020): 39135–39144, https://doi.org/10.1021/acsami.0c09948.

26. T. Mandai, Y. Youn, and Y. Tateyama, "Remarkable Electrochemical and Ion-Transport Characteristics of Magnesium-Fluorinated Alkoxyaluminate–diglyme Electrolytes for Magnesium Batteries," *Materials Advances* 2 (2021): 6283–6296, https://doi.org/10.1039/d1ma00448d.

27. T. Pavčnik, M. Lozinšek, K. Pirnat, et al., "On the Practical Applications of the Magnesium Fluorinated Alkoxyaluminate Electrolyte in Mg Battery Cells," *ACS Appl Mater Interfaces* 14 (2022): 26766–26774, https://doi.org/10.1021/acsami.2c05141.

28. T. Pavčnik, J. Imperl, M. Kolar, R. Dominko, and J. Bitenc, "Evaluating the Synthesis of $Mg[Al(hfip)_4]_2$ Electrolyte for Mg Rechargeable Batteries: Purity, Electrochemical Performance and Costs," *Journal of Materials Chemistry A* 12 (2024): 3386–3397, https://doi.org/10.1039/d3ta06378j.

29. N. T. Hahn, E. P. Kamphaus, Y. Chen, et al., "Magnesium Battery Electrolytes with Improved Oxidative Stability Enabled by Selective Solvation in Fluorinated Solvents," *ACS Applied Energy Materials* 6 (2023): 3264–3277, https://doi.org/10.1021/acsaem.2c03836.

30. Y. Sun, Y. Wang, L. Jiang, et al., "Non-Nucleophilic Electrolyte with Non-Fluorinated Hybrid Solvents for Long-Life Magnesium Metal Batteries," *Energy & Environmental Science* 16 (2022): 265–274, https://doi.org/10.1039/d2ee03235j.

31. C. Li, R. D. Guha, A. Shyamsunder, K. A. Persson, and L. F. Nazar, "A Weakly Ion Pairing Electrolyte Designed for High Voltage Magnesium Batteries," *Energy & Environmental Science* 17 (2023): 190–201, https://doi.org/10.1039/d3ee02861e.

32. Y. Du, Y. Chen, S. Tan, et al., "Strong Solvent Coordination Effect Inducing Gradient Solid-Electrolyte-Interphase Formation for Highly Efficient Mg Plating/Stripping," *Energy Storage Mater* 62 (2023): 102939, https://doi.org/10.1016/j.ensm.2023.102939.

33. H. A. Ishfaq, C. C. Cardona, E. Tchernychova, et al., "Transport Number Determination and Relevance for Lithium Metal Batteries Using Localized Highly Concentrated Electrolytes," *Chemistry of Materials* 37 (2025): 2485–2495, https://doi.org/10.1021/acs.chemmater.4c03067.

34. W. Xu, H. Wang, Y. Gao, et al., "A Localized High Concentration Electrolyte for 4 V-Class Potassium Metal Batteries," *Energy Advances* 1 (2022): 191–196, https://doi.org/10.1039/d2ya00015f.

35. Q. Liu, Y. H. Feng, X. Zhu, et al., "Stabilizing Cathode-Electrolyte Interphase by Localized High-Concentration Electrolytes for High-Voltage Sodium-Ion Batteries," *Nano Energy* 123 (2024): 109389, https://doi.org/10.1016/j.nanoen.2024.109389.

16146840, 2026, 18, Downloaded from https://advanced.onlinelibrary.wiley.com/doi/10.1002/aenm.202506415 by Ervin Rems - Bibliotheque de Sorbonne Universite , Wiley Online Library on [15/05/2026]. See the Terms and Conditions (https://onlinelibrary.wiley.com/terms-and-conditions) on Wiley Online Library for rules of use; OA articles are governed by the applicable Creative Commons License

36. T. Mandai, M. Yao, K. Sodeyama, A. Kagatsume, Y. Tateyama, and H. Imai, "Toward Improved Anodic Stability of Ether-Based Electrolytes for Rechargeable Magnesium Batteries," *Journal of Physical Chemistry C* 127 (2023): 10419–10433, https://doi.org/10.1021/acs.jpcc.3c01452.

37. J. Xiao, X. Zhang, H. Fan, et al., "Cosolvent-Assisted Formation of Charged Ion-Solvent Clusters and Solid Electrolyte Interphase for High-Performance Magnesium Metal Batteries," *Advanced Energy Materials* 12 (2022): 2202602, https://doi.org/10.1002/aenm.202202602.

38. H. A. Ishfaq, C. C. Cardona, E. Tchernychova, P. Johansson, R. Dominko, and S. Drvarič Talian, "Enhanced Performance of Lithium Metal Batteries via Cyclic Fluorinated Ether Based Electrolytes," *Energy Storage Mater* 69 (2024): 103375, https://doi.org/10.1016/j.ensm.2024.103375.

39. A. Marojević, T. Pavčnik, O. Lužanin, et al., "Influence of Salt Concentration on the Electrochemical Performance of Magnesium Hexafluoroisopropoxy Aluminate Electrolyte," *Batteries & Supercaps* 9 (2025): 202500497, https://doi.org/10.1002/batt.202500497.

40. S. Chen, Z. Yu, M. L. Gordin, R. Yi, J. Song, and D. Wang, "A Fluorinated Ether Electrolyte Enabled High Performance Prelithiated Graphite/Sulfur Batteries," *ACS Applied Materials & Interfaces* 9 (2017): 6959–6966.

41. S. Zhu and J. Chen, "Dual Strategy with Li-Ion Solvation and Solid Electrolyte Interphase for High Coulombic Efficiency of Lithium Metal Anode," *Energy Storage Mater* 44 (2022): 48–56, https://doi.org/10.1016/j.ensm.2021.10.007.

42. A. Baskin and D. Prendergast, "Exploration of the Detailed Conditions for Reductive Stability of $Mg(TFSI)_2$ in Diglyme: Implications for Multivalent Electrolytes," *The Journal of Physical Chemistry C* 120 (2016): 3583–3594, https://doi.org/10.1021/acs.jpcc.5b08999.

43. T. Liu, Y. Shao, G. Li, et al., "A Facile Approach Using $MgCl_2$ to Formulate High Performance Mg^{2+} Electrolytes for Rechargeable Mg Batteries," *Journal of Materials Chemistry A* 2 (2014): 3430–3438, https://doi.org/10.1039/c3ta14825d.

44. S. He, K. V. Nielson, J. Luo, and T. L. Liu, "Recent Advances on $MgCl_2$ Based Electrolytes for Rechargeable Mg Batteries," *Energy Storage Mater* 8 (2017): 184–188, https://doi.org/10.1016/j.ensm.2016.12.001.

45. S. Ilic, S. N. Lavan, N. J. Leon, et al., "Mixed-Anion Contact Ion-Pair Formation Enabling Improved Performance of Halide-Free Mg-Ion Electrolytes," *ACS Applied Materials & Interfaces* 16 (2024): 435–443, https://doi.org/10.1021/acsami.3c11293.

46. M. Salama, I. Shterenberg, H. Gizbar, et al., "Unique Behavior of Dimethoxyethane (DME)/$Mg(N(SO_2CF_3)_2)_2$ Solutions," *The Journal of Physical Chemistry C* 120 (2016): 19586–19594, https://doi.org/10.1021/acs.jpcc.6b07733.

47. D. M. Driscoll, N. K. Dandu, N. T. Hahn, et al., "Rationalizing Calcium Electrodeposition Behavior by Quantifying Ethereal Solvation Effects on Ca^{2+} Coordination in Well-Dissociated Electrolytes," *Journal of The Electrochemical Society* 167 (2020): 160512.

48. M. Salama, I. Shterenberg, Y. Gofer, and D. Aurbach, "$MgTFSI_2/MgCl_2$ /DME Solution Structure Analysis," *Electrochemical Society Meeting Abstracts* MA2018-01 (2018): 261, https://doi.org/10.1149/ma2018-01/3/261.

49. C. Li, A. Shyamsunder, B. Key, Z. Yu, and L. F. Nazar, "Stabilizing Magnesium Plating by a Low-Cost Inorganic Surface Membrane for High-Voltage and High-Power Mg Batteries," *Joule* 7 (2023): 2798–2813, https://doi.org/10.1016/j.joule.2023.10.012.

50. R. Attias, B. Dlugatch, M. S. Chae, Y. Goffer, and D. Aurbach, "Changes in the Interfacial Charge-Transfer Resistance of Mg Metal Electrodes, Measured by Dynamic Electrochemical Impedance Spectroscopy," *Electrochemistry Communications* 124 (2021): 106952.

51. J. Tang and F. Xu, "Polyaniline Cathode for Dual-Ion Rechargeable Mg Batteries," *Materials Letters* 320 (2022): 132365, https://doi.org/10.1016/j.matlet.2022.132365.

52. M. Li, R. P. Hicks, Z. Chen, et al., "Electrolytes in Organic Batteries," *Chemical Reviews* 123 (2023): 1712–1773.

53. X. He, R. Cheng, X. Sun, et al., "Organic Cathode Materials for Rechargeable Magnesium-Ion Batteries: Fundamentals, Recent Advances, and Approaches to Optimization," *Journal of Magnesium and Alloys* 11 (2023): 4359–4389.

54. O. Lužanin, J. Moškon, T. Pavčnik, R. Dominko, and J. Bitenc, "Unveiling True Limits of Electrochemical Performance of Organic Cathodes in Multivalent Batteries through Cyclable Symmetric Cells," *Batteries & Supercaps* 6 (2023): 202200437, https://doi.org/10.1002/batt.202200437.

55. H. Wang, X. Feng, Y. Chen, et al., "Reversible Electrochemical Interface of Mg Metal and Conventional Electrolyte Enabled by Intermediate Adsorption," *ACS Energy Letters* 5 (2020): 200–206, https://doi.org/10.1021/acsenergylett.9b02211.

56. S. Drvarič Talian, G. Kapun, J. Moškon, R. Dominko, and M. Gaberšček, "Operando Impedance Spectroscopy with Combined Dynamic Measurements and Overvoltage Analysis in Lithium Metal Batteries," *Nature Communications* 16 (2025): 2030.

57. K. H. Chen, K. N. Wood, E. Kazyak, et al., "Dead Lithium: Mass Transport Effects on Voltage, Capacity, and Failure of Lithium Metal Anodes," *Journal of Materials Chemistry A* 5 (2017): 11671–11681, https://doi.org/10.1039/c7ta00371d.

58. S. Fan, S. Cora, and N. Sa, "Evolution of the Dynamic Solid Electrolyte Interphase in Mg Electrolytes for Rechargeable Mg-Ion Batteries," *ACS Appl Mater Interfaces* 14 (2022): 46635–46645, https://doi.org/10.1021/acsami.2c13037.

59. M. P. Gomes, I. Costa, N. Pébère, J. L. Rossi, B. Tribollet, and V. Vivier, "On the Corrosion Mechanism of Mg Investigated by Electrochemical Impedance Spectroscopy," *Electrochimica Acta* 306 (2019): 61–70, https://doi.org/10.1016/j.electacta.2019.03.080.

60. M. Esmaily, J. E. Svensson, S. Fajardo, et al., "Fundamentals and Advances in Magnesium Alloy Corrosion," *Progress in Materials Science* 89 (2017): 92–193, https://doi.org/10.1016/j.pmatsci.2017.04.011.

61. T. Purkait, M. Radi, C. Bodin, R. Dedryvere, and A. Ponrouch, "A Comprehensive Study of the Parameters Affecting Magnesium Plating/Stripping Kinetics in Rechargeable Mg Batteries," *Electrochemical Society Meeting Abstracts* MA2023-02 (2023): 616, https://doi.org/10.1149/ma2023-024616mtgabs.

62. D. T. Nguyen, A. Y. S. Eng, M. F. Ng, et al., "A High-Performance Magnesium Triflate-Based Electrolyte for Rechargeable Magnesium Batteries," *Cell Reports Physical Science* 1 (2020): 100265, https://doi.org/10.1016/j.xcrp.2020.100265.

63. A. Kopač Lautar, J. Bitenc, T. Rejec, R. Dominko, J. S. Filhol, and M. L. Doublet, "Electrolyte Reactivity in the Double Layer in Mg Batteries: an Interface Potential-Dependent DFT Study," *Journal of the American Chemical Society* 142 (2020): 5146–5153, https://doi.org/10.1021/jacs.9b12474.

64. S. Drvarič Talian, J. Bobnar, A. R. Sinigoj, I. Humar, and M. Gaberšček, "Transmission Line Model for Description of the Impedance Response of Li Electrodes with Dendritic Growth," *Journal of Physical Chemistry C* 123 (2019): 27997–28007, https://doi.org/10.1021/acs.jpcc.9b05887.

65. R. Narayan, A. Blagojević, G. Mali, et al., "Nanostructured Poly(hydroquinonyl-benzoquinonyl sulfide)/Multiwalled Carbon Nanotube Composite Cathodes: Improved Synthesis and Performance for Rechargeable Li and Mg Organic Batteries," *Chemistry of Materials* 34 (2022): 6378–6388, https://doi.org/10.1021/acs.chemmater.2c00862.

66. B. D. Adams, J. Zheng, X. Ren, W. Xu, and J. G. Zhang, "Accurate Determination of Coulombic Efficiency for Lithium Metal Anodes and Lithium Metal Batteries," *Advanced Energy Materials* 8 (2018): 1702097, https://doi.org/10.1002/aenm.201702097.

67. N. Fairley and A. Carrick, "The Casa Cookbook," *Casa Software Limited* (2005) .

16146840, 2026, 18, Downloaded from https://advanced.onlinelibrary.wiley.com/doi/10.1002/aenm.202506415 by Ervin Rems - Bibliotheque de Sorbonne Universite , Wiley Online Library on [15/05/2026]. See the Terms and Conditions (https://onlinelibrary.wiley.com/terms-and-conditions) on Wiley Online Library for rules of use; OA articles are governed by the applicable Creative Commons License

68. D. J. Morgan, "XPS Insights: Asymmetric Peak Shapes in XPS," *Surface and Interface Analysis* 55 (2023): 567–571, https://doi.org/10.1002/sia.7215.

69. M. J. Frisch, G. W. Trucks, H. B. Schlegel, et al., "Gaussian 09 Revision A.1. Gaussian Inc," *Wallingford CT* (2009).

70. C. G. Zhan, J. A. Nichols, and D. A. Dixon, "Ionization Potential, Electron Affinity, Electronegativity, Hardness, and Electron Excitation Energy: Molecular Properties from Density Functional Theory Orbital Energies," *The Journal of Physical Chemistry A* 107 (2003): 4184–4195, https://doi.org/10.1021/jp0225774.

71. Z. Zhang, L. Hu, H. Wu, et al., "Fluorinated Electrolytes for 5 V Lithium-Ion Battery Chemistry," *Energy & Environmental Science* 6 (2013): 1806–1810, https://doi.org/10.1039/c3ee24414h.

72. S. Plimpton, "Fast Parallel Algorithms for Short-Range Molecular Dynamics," *Journal of Computational Physics* 117 (1995): 1–19, https://doi.org/10.1006/jcph.1995.1039.

73. W. L. Jorgensen, D. S. Maxwell, and J. Tirado-Rives, "Development and Testing of the OPLS All-Atom Force Field on Conformational Energetics and Properties of Organic Liquids," *Journal of the American Chemical Society* 118 (1996): 11225–11236, https://doi.org/10.1021/ja9621760.

74. W. L. Jorgensen and J. Tirado-Rives, "Potential Energy Functions for Atomic-Level Simulations of Water and Organic and Biomolecular Systems," *Proceedings of the National Academy of Sciences* 102 (2005): 6665–6670, https://doi.org/10.1073/pnas.0408037102.

75. L. S. Dodda, I. C. De Vaca, J. Tirado-Rives, and W. L. Jorgensen, "LigParGen Web Server: an Automatic OPLS-AA Parameter Generator for Organic Ligands," *Nucleic Acids Research* 45 (2017): W331–W336, https://doi.org/10.1093/nar/gkx312.

76. L. S. Dodda, J. Z. Vilseck, J. Tirado-Rives, and W. L. Jorgensen, "1.14*CM1A-LBCC: Localized Bond-Charge Corrected CM1A Charges for Condensed-Phase Simulations," *The Journal of Physical Chemistry B* 121 (2017): 3864–3870, https://doi.org/10.1021/acs.jpcb.7b00272.

77. A. A. H. Pádua, "Resolving Dispersion and Induction Components for Polarisable Molecular Simulations of Ionic Liquids," *Journal of Chemical Physics* 146 (2017): 204501, https://doi.org/10.1063/1.4983687.

78. J. Self, K. D. Fong, and K. A. Persson, "Transport in Superconcentrated $LiPF_6$ and $LiBF_4$/Propylene Carbonate Electrolytes," *ACS Energy Letters* 4 (2019): 2843–2849, https://doi.org/10.1021/acsenergylett.9b02118.

79. Z. Yu, P. E. Rudnicki, Z. Zhang, et al., "Rational Solvent Molecule Tuning for High-Performance Lithium Metal Battery Electrolytes," *Nature Energy* 7 (2022): 94–106, https://doi.org/10.1038/s41560-021-00962-y.

Supporting Information

Additional supporting information can be found online in the Supporting Information section.

Supporting File: aenm70801-sup-0001-SuppMat.docx.

16146840, 2026, 18, Downloaded from https://advanced.onlinelibrary.wiley.com/doi/10.1002/aenm.202506415 by Ervin Rems - Bibliothèque de Sorbonne Université , Wiley Online Library on [15/05/2026]. See the Terms and Conditions (https://onlinelibrary.wiley.com/terms-and-conditions) on Wiley Online Library for rules of use; OA articles are governed by the applicable Creative Commons License